Direct simulations and subgrid modeling of turbulent channel flows asymmetrically heated from both walls

M. David, Adrien Toutant, Françoise Bataille

Direct simulations and subgrid modeling of turbulent channel flows asymmetrically heated from both walls

M.David,[1, a)] A.Toutant,[1, b)] and F. Bataille[1, c)]
PROMES-CNRS laboratory (UPR 8521), Université de Perpignan via Domitia, Technosud-Rambla de la thermodynamique, 66100 Perpignan, France

(Dated: 13 July 2021)

Thermal Large-Eddy Simulations (T-LES) and a Direct Numerical Simulation (DNS) are carried out in a bi-periodical channel with hot and cold wall temperatures of respectively 900 K and 1300 K. The mean fluid temperature is lowered below the cold wall temperature thanks to a heat source, resulting in a both walls heating of the fluid. The hot and cold wall friction Reynolds numbers are respectively 640 and 1000. These conditions are representative of the working conditions of gas-pressurized solar receiver of solar power tower. The Low Mach number Navier-Stokes equations are solved. The coupling between the dynamic and the temperature effects is considered. In the T-LES, both the momentum convection and the density-velocity correlation subgrid terms are modeled. Functional models, structural models, and mixed models are considered. A tensorial version of the Anisotropic Minimum-Dissipation (AMD) model is also investigated. The Quick and the second-order centered schemes are tested for the discretization of the mass convection term. Firstly, an overview of the results of 17 T-LES on first- and second-order statistics is proposed. It permits selecting 6 of these simulations for a detailed analysis consisting in the investigation of profiles of mean quantities and turbulent correlations. A particular attention is given to the wall heat fluxes because it is a critical point for the design and the optimization of solar receivers. Overall, the first-order statistics are better predicted than the second-order's. The tensorial AMD model takes advantage of the classical AMD model properties and better reproduces the anisotropy of the flow thanks to its formulation. The tensorial AMD model produces the most reliable and efficient results among the considered models.

I. INTRODUCTION

This paper addresses the low Mach-number Thermal Large-Eddy Simulation (T-LES) of strongly anisothermal turbulent channel flows heated from both sides. The studied conditions are commonly encountered in many industrial processes such as heat exchangers, nuclear reactors[1,2], thermal solar systems[3–5]. Particularly, in the field of concentrated solar power, the solar receiver is a key component. It aims to convert solar radiation into heat of the transfer fluid. Solar receivers are characterized by an intense turbulence and a strong asymmetric heating of the fluid. The academic channel geometry is well adapted to reproduce these characteristics and has been selected. Several studies are conducted to optimize it[6,7]. To this end, it is necessary to (1) deepen our understanding of the kind of flow and (2) provide reliable means to test proposed optimizations. With the increase of computing capacity, simulations have emerged to play a major role in the research of wall-bounded turbulence. In 1987, Kim *et al.*[8] were among the first authors to provide reliable turbulence statistics in fully developed channel flows. A large number of studies dealing with isothermal turbulent flows at mean Reynolds numbers inferior or equal to 395 have been carried out since then[9–11]. Direct numerical simulations of highly turbulent channel flow are more recent[12–16]. Simulation of anisothermal turbulent channel flows are even newer. Kawamura[17] performed DNS of turbulent heat transfer in channel flow with respect to Reynolds and Prandtl number effects. The temperature was, however, a passive scalar. Few studies take into account the coupling between turbulence and temperature. For instance, Dupuy *et al.*[18,19] and Aulery *et al.*[20] investigated channel flows at friction Reynolds numbers of 180 and 395. Recently, David *et al.*[21] performed a DNS of an anisothermal channel flow at a friction Reynolds of 970. In these studies, the fluid temperature was close to the average of the wall temperatures, meaning that the fluid was heated by one wall and cooled by the other. In most industrial applications, the fluid is heated on both sides. For these reasons, in this study we carry out a DNS at a friction Reynolds of 1000 with a mean fluid temperature lower than the wall temperature. This simulation is representative of the working conditions encountered in gas-pressurized solar receivers of solar power towers and in many systems involving heat exchangers.

Currently, the computational cost of the DNS renders the simulation of turbulent flow associated with complex geometries unfeasible. The LES is a family of methods aiming to obtain a low-cost three-dimensional unsteady simulation of a turbulent flow. The reader is referred to Ref.[22] for a quick overview of its history and a review of its current state. In LES, large scales are explicitly resolved, while small scales, more computationally expensive to resolve, are accounted for by their modeled influences on larger turbulent structures. Generally, the scale separation is performed with implicit filtering meaning that, the grid is the LES low-pass filter. Subgrid-scale models must be used to close the governing equations of the filtered fields. They should follow physical and numerical constraints relying on the idea that subgrid-scale models have to be consistent with important mathematical and physical properties of the Navier-Stokes equations and the turbulent stresses. The subgrid model should conserve

[a)]Electronic mail: martin.david@promes.cnrs.fr
[b)]Electronic mail: Author to whom correspondence should be addressed: adrien.toutant@promes.cnrs.fr
[c)]Electronic mail: francoise.bataille@promes.cnrs.fr

the basic properties of the Navier-Stokes equations, induce the same type of effect as the modeled term, and allow the flow driving mechanisms. It should also vanish if there is no subgrid-scale. Among the numerical constraints, the subgrid-scale model should not alter the stability of the simulation[23]. Silvis *et al.*[24] detail the symmetry requirements, the desired near-wall scaling behavior of the subgrid-scale stresses, the realizability constraints, and requirements on the production of subgrid-scale kinetic energy. They show that certain model constraints are not compatible with each other.

On a classical LES grid, the balance between convective transport and diffusive dissipation, which is the driving force of turbulence, is deteriorated. The success of a turbulence model depends on its ability to capture and compensate this imbalance. Zero-equation models assume that the small scales are universal and can be computed with the resolved flow variables. The LES models are usually divided into two groups. (1) Functional models consist in reproducing the action of the small scales by introducing a subgrid viscosity that has a similar effect on the bigger turbulent scales. Functional approaches are specifically designed to reproduce the same effect as the exact term on the resolved physics. However, they often are over-dissipating since they do not model the backward of the energy cascade. Some of the most used functional models are given below. The Smagorinsky model[25] is probably the most known of the functional models since it is the first developed eddy-viscosity model. It is very simple to implement but significantly over-dissipative. Nonetheless, a large number of newer models rely on the Smagorinsky model basis. The Wall-Adapting Local Eddy-viscosity (WALE) model[26] is dedicated to complex geometries. It involves the square of the velocity gradient tensor to model the strain and the rotation rate of the smallest resolved turbulent fluctuations. The WALE model has been deeply analyzed by Kim *et al.*[27] in the canonical transitional boundary layer, producing good results. Nicoud *et al.*[28] propose the σ-model which is derived from the analysis of the singular values of the resolved velocity gradient tensor. It can be used in flows with non-homogeneous directions in space or time. The σ-model appears to be particularly efficient for wall-bounded flows. The Anisotropic Minimum-Dissipation model (AMD)[29] takes advantage of the desirable practical and theoretical properties of the QR model[30] and is applicable on anisotropic grids. This model gives the minimum eddy dissipation required to dissipate the energy of sub-filter scales. It appropriately switches off in laminar and transitional flows and is consistent with the exact subfilter stress tensor on both isotropic and anisotropic grids. The AMD model gives good agreement with DNS in turbulent channel flows[9,19,21].

The Kobayashi model[31] relies on coherent structures for rotating homogeneous turbulence and turbulent channel flow. It gives similar results as the Smagorinsky results in the common LES test case but does not require to average or clip the model parameter, use an explicit wall-damping function, or modify the fixed parameter. Vreman[32] proposes a model that is characterized by a relatively small dissipation in transitional and near-wall regions that, as the Kobayashi model, does not involve averaging, or clipping procedures, explicit filtering, and is invariant by rotation for isotropic filter widths. Trias *et al.*[33] propose a general framework for eddy-viscosity models based on a 5D phase space of invariants. They build three invariants of the second-order tensor GG^T, where G is the gradient tensor, and use them to derive the S3PQR model. A model based on the second-order volumetric strain-stretching (VSS) tensor is proposed by Ryu and Iaccarino[34]. It is tested in freely decaying isotropic turbulence, incompressible turbulent channel flow, and compressible turbulent channel flows. Studying LES of incompressible flows, Silvis *et al.*[24] express a model based on the vortex stretching magnitude which respects all the properties listed in its paper except the nonzero subgrid dissipation for non-laminar flow types and the sufficient subgrid dissipation for scale separation. The structure-function model[35] relies on a kinetic energy spectrum local in space, calculated thanks to a local second-order velocity structure-function, to compute the spectral eddy-viscosity. This model is a generalization of the spectral eddy-viscosity to highly intermittent situations in physical space. Tensorial subgrid viscosities are formulated to deal with anisotropic turbulence. The spectral model proposed by Aupoix[36] includes all the coupling mechanisms between large and small scales. Pressure and transfer effects are defined as integrals over the subgrid scales. However, it induces high computational costs. Horuiti[37] extends the Smagorinsky model to the anisotropic case. The third-order terms in an anisotropic representation model of the Reynolds stresses are used to determine the eddy-viscosity velocity scale. Dupuy *et al.*[9] propose various tensorial viscosity computed with the AMD model. The $H^{(4)}$ version tested in Refs.[9,18,19,21] produces encouraging results. (2) Structural models aim at approximating the subgrid tensor by constructing it from an evaluation of the filtered velocity or a formal series expansion[23]. The advantage of starting from the exact unclosed expression of the term to model is that the resulting closure often shares a similar structure with the exact term. They do not suppose that the small structures always drain energy from the large scales, and they can predict the exact subgrid-scale terms more accurately than eddy-viscosity models. Hence, they could enhance the capture of anisotropic effects and the prediction of energy transfer and disequilibrium. Drawbacks of structural models are generally a poor prediction of the dissipation and their inclination to be unstable[23]. The reader is referred to the review of structural models proposed by Lu and Rutland[38].

Mixed modeling relies on the linear combination of the functional and structural approaches. It aims to take advantage of the generally good estimation of the energy transfer between the resolved and the subgrid scales of the functional models and to benefit from the accurate prediction of the subgrid tensor obtained with structural models. Mixed models show encouraging results in various tests Refs.[37,39–43]. Streher *et al.*[44] propose a two-layer mixed model for the LES of isothermal channel flow: the near-wall region is parameterized with the combination of the AMD and the scale similarity model[45], whereas the outer region is computed with the scale similarity model only. The obtained results are in very good agreement with the DNS of Moser *et al.*[12] and Hoyas and Jiménez[15].

In anisothermal flows, the temperature variations impact the turbulence and *vice-versa* which renders the simulation of such flows more complicated[46–50]. The asymmetric heating of the flow induces specific turbulent structures on both sides of the channel. The high heat fluxes are linked to high-frequency turbulent scales and strong wall-normal velocities. In those conditions, the density-velocity correlation term is not negligible anymore and requires to be modeled in addition to the velocity-velocity correlation term classically modeled [18]. The modeling of the subgrid-scale heat flux in LES for turbulent thermal flows has often been based on the hypothesis of Eidson[51] which assumes that the energy transfer from the resolved scales to the subgrid scales is proportional to the gradient of resolved temperature. The subgrid-scale thermal diffusivity is traditionally represented based on the Reynolds analogy and the concept of turbulent Prandtl number. Rasam *et al.*[52] propose an explicit algebraic subgrid scalar flux model based on the modeled transport equation of the subgrid-scale scalar flux. It is strongly dependent on the accuracy of the subgrid-scale stress prediction. The obtained turbulent scalar flux is not necessarily aligned with the resolved scalar gradient. Furthermore, the inherent dependence on the resolved rotation-rate tensor renders the model suitable for LES of rotating flow applications. Wang *et al.*[53–55] develop a series of models which includes the resolved strain-rate tensor, the rotation rate tensor, and the temperature gradient. Contrary to the classical dynamic eddy thermal diffusivity subgrid-scale heat flux model, the three new models proposed in this study admit more degrees of freedom and consequently provide a more realistic geometrical and physical representation of the subgrid-scale heat flux vector. Peng and Davidson[56] propose a model that accounts for the subgrid-scale heat flux in terms of the large-scale strain rate and the temperature gradient in all directions, which is equivalent to using a tensor diffusivity. The proposed model formulates the subgrid-scale heat flux. Hence, it allows the large-scale thermal gradient in other directions to modify the subgrid-scale heat flux in the direction with no statistical temperature gradient. The minimum-dissipation scalar transport model is an extension of the AMD model proposed by Rozema[29]. This model is successfully tested in a thermally stratified atmospheric boundary layer flows by Abkar and Moin[57]. Particularly, it accurately estimates the expected surface-layer similarity profiles and power spectra for both velocity and scalar concentration. Ries *et al.*[58] suggest a wall-adapted anisotropic heat flux model. It is designed for complex turbulent thermal flow. The model accounts for variable fluid properties and anisotropic effects in the unresolved temperature scales; does not require *ad-hoc* treatments or dynamic procedure to obtain the correct near-wall behavior; its formulation is consistent with the second law of thermodynamics.

This study follows up on a previous paper focused on anisothermal turbulent channel flow heated from one side and cooled from the other[21]. The results are extended regarding the new working conditions inducing a stronger wall heat flux on the hot side and an opposed direction of the heat transfer at the cold wall. The objective of this work is twofold: provide reference data of a turbulent channel flow strongly and asymmetrically heated from both sides and assess a large number of LES models in those conditions thanks to *a posteriori* tests.

The organization of this paper is as follows: Sec. II describes the resolved equations. The investigated subgrid-scale models are detailed in Sec. III. The channel flow configuration and the numerical method are presented in Sec. IV. In Sec. V, the results of the present DNS are compared with those of the DNS performed at similar friction Reynolds numbers but different thermal conditions by David *et al.*[21]. Then, the Thermal Large-Eddy Simulations (T-LES) are investigated: the global efficacy of the T-LES are presented and six of them are subjected to detailed analysis . A final section concludes.

II. FILTERED LOW-MACH NUMBER EQUATIONS

We consider the large-eddy simulation of the low Mach number equations in the Favre formulation as described in the work of David *et al.*[21]. The Favre formulation involves Favre-filtered variables, based on the density-weighted Favre filter ($\widetilde{\cdot}$). For any field ψ, the variables are expressed as $\widetilde{\psi} = \overline{\rho\psi}/\overline{\rho}$, where ($\overline{\cdot}$) is the unweighted classical filter. The two most significant subgrid terms highlighted by Dupuy *et al.*[18] are modeled: a subgrid term related to the velocity-velocity correlation and another modeling the density-velocity correlation. The Navier-Stokes are solved under the low-Mach number approximation, which admits large variations in gas density while remains acoustically incompressible[59]. This hypothesis, well adapted to the studied conditions, introduces two pressures: the mechanical pressure, which is the relative pressure and is variable in space, and the thermodynamical pressure, which is the reference static pressure and is homogeneous. In the used algorithm the mechanical pressure is computed from the constraint equation of the velocity divergence. The low-Mach number is assumed to be valid for Mach numbers below 0.3. In the studied configuration, the Mach number is 0.12. The resolution of the Navier-Stokes equations under the low-Mach number approximation permits to lower the computational cost of simulations by increasing the fractional timestep when compared to the resolution of the compressible Navier-Stokes equations. In the simulations, the computation of the diffusion is explicit. The timestep is computed at each iteration to respect the stability criterion. In the studied configuration, the diffusion timestep is smaller than the convection timestep. The LES and DNS diffusion time steps are close because the size of the first cell is similar in both simulations. Indeed, in the achieved LES the viscous sublayer is resolved. All the turbulence time scales are expected to be captured: the simulated time is about 0.1 s and the diffusion timestep is about $3 \cdot 10^{-8}$ s, resulting in a ratio between the two quantities of $3 \cdot 10^{6}$. In this study, the Stokes' hypothesis is assumed. The reader is referred to Ref.[60] for precise explanations on the applicability of the Stokes' hypothesis to low Mach number flows. A source term is introduced in the energy equation to allow the study of different axial locations in a solar receiver by modifying the fluid temperature. The bigger the source term is, the lower the fluid temperature is, traducing a location closer to the inlet of a solar receiver.

This source term is homogeneous all over the computational domain and constant in time. It has been set to 55 MW/m^3 to obtain a mean fluid temperature below but near the cold wall temperature which is representative of close to the outlet fluid temperature in gas-pressurized solar receivers. The low-Mach number Navier-Stokes equations are given below.

- Mass conservation equation:

$$\frac{\partial \overline{\rho}}{\partial t} + \frac{\partial \overline{\rho}\widetilde{U}_j}{\partial x_j} = 0, \tag{1}$$

- Momentum conservation equation:

$$\frac{\partial \overline{\rho}\widetilde{U}_i}{\partial t} = -\frac{(\partial \overline{\rho}\widetilde{U}_j\widetilde{U}_i + \overline{\rho}G_{U_jU_i})}{\partial x_j} - \frac{\partial \overline{P}}{\partial x_i} + \frac{\partial \Sigma_{ij}(\widetilde{\boldsymbol{U}},\widetilde{T})}{\partial x_j}, \tag{2}$$

- Energy conservation equation:

$$\frac{\partial(\widetilde{U}_j + \overline{\rho}G_{Uj/\rho})}{\partial x_j} = -\frac{1}{\gamma P_0}\left[(\gamma-1)\left(\frac{\partial Q_j(\widetilde{T})}{\partial x_j} - H_s\right) + \frac{\mathrm{d}P_0}{\mathrm{d}t}\right], \tag{3}$$

- Ideal gas law:

$$\widetilde{T} = \frac{P_0}{\overline{\rho} r}, \tag{4}$$

where ρ is the density, T is the temperature, $\gamma = 1.33$ is the heat capacity ratio of air at 1100 K, r is the ideal gas specific constant, t is the time, P is the mechanical pressure, P_0 the thermodynamical pressure, U_i is the ith component of velocity, $\mathrm{d}/\mathrm{d}t$ is the time derivative (total derivative since P_0 is homogeneous), and x_i is the Cartesian coordinate in the ith direction. $H_s = 55$ MW/m^3 is the source term. The volume of the studied channel is 2.8×10^{-6} m^3. The source term is chosen to represent a fluid temperature in the range of the experimental working conditions of a solar receiver. The obtained mean fluid temperature is below the cold wall temperature leading to fluid heated from both sides. The subgrid term relative to momentum convection is $G_{U_jU_i} = \widetilde{U_jU_i} - \widetilde{U}_j\widetilde{U}_i$ and the subgrid term relative to the density-velocity correlation is expressed as $G_{U_j/\rho} = \widetilde{U_j/\rho} - \widetilde{U}_j/\overline{\rho}$. This last term is beneficial for the prediction of temperature-related statistics[19]. The Einstein summation convention is used. The shear-stress tensor and conductive heat flux associated with a given velocity and temperature are computed with the functions $\Sigma_{ij}(\widetilde{\boldsymbol{U}},\widetilde{T})$ and $Q_j(\widetilde{T})$. The particular form of the energy conservation equation, involving the velocity divergence, is obtained as follows. The ideal gas law is applied to the energy equation written in terms of transport of temperature. Then, the homogeneity property of the thermodynamical pressure is used. This formulation of the energy conservation equation is also used in Refs.[19,21,61]. The coupling between the thermodynamic pressure, the density, and the temperature are considered thanks to the ideal gas law. The thermodynamical pressure is obtained by integrating Eq. 3 over the volume of the computational domain:

$$\frac{\mathrm{d}P_0}{\mathrm{d}t} = -(\gamma-1)\left(\frac{1}{V}\int Q_j(\widetilde{T})\mathrm{d}S_j - H_s\right) \tag{5}$$

where V is the volume of the computational domain and S_j are the boundaries of the computational domain.

Newtonian fluid and Fourier's law are assumed, leading to the following expressions:

$$\Sigma_{ij}(\widetilde{\boldsymbol{U}},\widetilde{T}) = \mu(\widetilde{T})\left(\frac{\partial \widetilde{U}_i}{\partial x_j} + \frac{\partial \widetilde{U}_j}{\partial x_i}\right) - \frac{2}{3}\mu(\widetilde{T})\frac{\partial \widetilde{U}_k}{\partial x_k}\delta_{ij}, \tag{6}$$

$$Q_j(\widetilde{T}) = -\lambda(\widetilde{T})\frac{\partial \widetilde{T}}{\partial x_j}, \tag{7}$$

with $\mu(\widetilde{T})$ the dynamic viscosity, $\lambda(\widetilde{T})$ the thermal conductivity, and δ_{ij} the Kronecker symbol.

The fluid used is air. The viscosity is computed using the Sutherland's law[62]:

$$\mu(\widetilde{T}) = \mu_0\frac{\widetilde{T}}{T_0}^{3/2}\frac{T_0+S}{\widetilde{T}+S}, \tag{8}$$

where $\mu_0 = 1.716\times10^{-5}\ Pa\cdot s$, $S = 110.4$ K, and $T_0 = 273.15$ K. The Prandtl number is supposed to be constant, Pr$=0.87$ and the heat capacity at constant pressure $C_p = 1155\ \mathrm{J\cdot kg^{-1}\cdot K^{-1}}$. The conductivity is deduced from the Prandtl number, the heat capacity at constant pressure, and the viscosity:

$$\lambda(\widetilde{T}) = \frac{C_p}{\mathrm{Pr}}\mu(\widetilde{T}). \tag{9}$$

III. SUBGRID-SCALE MODELING

In this section, each type of modeling is presented and the construction of the models is given. The models for the velocity-velocity correlation subgrid term and density-velocity correlation subgrid term are expressed as follows:

$$G_{U_jU_i} \approx \tau_{ij}^{mod}(\widetilde{\boldsymbol{U}},\overline{\Delta}), \tag{10}$$

$$G_{U_j/\rho} \approx \pi_j^{mod}(\widetilde{\mathbf{U}},1/\overline{\rho},\overline{\Delta}). \tag{11}$$

The subgrid-scale tensors, τ_{ij} and π_j, are computed thanks to variables resolved in T-LES. Each model has its proper expression of the subgrid-scale tensors. The considered models are detailed below. This includes functional models and structural models. Note that in the following of this article, the filter length scale is computed using the mesh size in the three directions $\overline{\Delta} = \left(\overline{\Delta}_x\overline{\Delta}_y\overline{\Delta}_z\right)^{1/3}$. Since no explicit filter is used, the filter length scale and the mesh size are combined.

A. Functional modeling

Functional models introduce an artificial subgrid viscosity which accounts for the effect of the non-resolved small turbulence scales. The subgrid-stress tensor relative to the velocity-velocity correlation is expressed as follows:

$$\tau_{ij}^{mod}(\widetilde{U},\overline{\Delta}) = -2\nu_t^{mod}(\mathbf{g},\mathbf{d},\overline{\Delta})S_{ij}, \tag{12}$$

where $S_{ij} = 0.5(g_{ij}+g_{ji})$ is the rate of the deformation tensor, $\mathbf{g}$ is the velocity gradient, expressed as $g_{ij} = \partial\widetilde{U}_i/\partial x_j$, and ν_t^{mod} is the turbulent viscosity and is specific to each model. The density-velocity subgrid term is computed with eddy-diffusivity models. They involve the turbulent Prandtl number, $\mathrm{Pr_t}$:

$$\pi_j^{mod}(\widetilde{U},\phi,\overline{\Delta}) = -\frac{\nu_t^{mod}(\mathbf{g},\mathbf{d},\overline{\Delta})}{\mathrm{Pr_t}}d_j, \tag{13}$$

with $\boldsymbol{d_j} = \partial\phi/\partial x_j$ the scalar gradient. $\mathrm{Pr_t} = 0.9$ is the turbulent Prandtl number, defined as the ratio between the momentum eddy-diffusivity and the heat transfer eddy-diffusivity.

The following functional models are investigated in this study.

- WALE model[26]:

$$\nu_t^{WALE}\left(\mathbf{g},\mathbf{d},\overline{\Delta}\right) = \left(C^{WALE}\overline{\Delta}\right)^2\frac{\left(S_{ij}^dS_{ij}^d\right)^{3/2}}{\left(S_{mn}S_{mn}\right)^{5/2}+\left(S_{mn}^dS_{mn}^d\right)^{5/4}}, \tag{14}$$

- AMD model[29]:

$$\nu_t^{AMD}\left(\mathbf{g},\mathbf{d},\overline{\Delta}\right) = C^{AMD}\frac{max(0,-G_{ij}S_{ij})}{g_{mn}g_{mn}}, \tag{15}$$

- Scalar AMD model[57]:

$$\nu_t^{AMD}\left(\mathbf{g},\mathbf{d},\overline{\Delta}\right) = C^{AMDs}\frac{max(0,-D_jd_j)}{d_md_m}, \tag{16}$$

- Sigma model[28]:

$$\nu_t^{Sigma}\left(\mathbf{g},\mathbf{d},\overline{\Delta}\right) = \left(C^{Sigma}\overline{\Delta}\right)^2\frac{\sigma_3(\sigma_1-\sigma_2)(\sigma_2-\sigma_3)}{\sigma_1^2}, \tag{17}$$

with S_{ij}^d the traceless symmetric part of the squared velocity gradient tensor, $\sigma_1 > \sigma_2 > \sigma_3$ the three singular values of $\mathbf{g}$, $G_{ij} = \overline{\Delta_k}^2 g_{ik}g_{jk}$ the gradient model, and $D_j = \overline{\Delta_k}^2 g_{jk}d_k$ the gradient model for the density-velocity correlation subgrid term. Unless otherwise is stated, the functional model constants used are $C^{WALE} = 0.55$, $C^{AMD} = 0.3$, $C^{AMDs} = 0.3$, and $C^{Sigma} = 1.5$.

The modeling of the subgrid scale requires to preserve the generic properties of the filtered Navier-Stokes equations. Deville *et al.*[63] gives the expression that the stress tensor should follow to conserve the invariance properties:

$$\begin{aligned}\tau_{ij} =& a\left(\mathbf{S_{ij}}\cdot\gamma\otimes\gamma+\gamma\otimes\gamma\cdot\mathbf{S_{ij}}\right)+b\,\gamma\otimes\gamma\cdot\mathbf{S_{ij}}\cdot\gamma\otimes\gamma+c\,\mathbf{S_{ij}}\\ &+\left(d\,tr(\mathbf{S_{ij}})+e\,\mathbf{S_{ij}}:\gamma\otimes\gamma\right)\mathbf{I}+e\,tr(\mathbf{S_{ij}}\gamma\otimes\mathbf{e}),\end{aligned} \tag{18}$$

with γ the unit vector used to represent the axes of a Cartesian coordinate system, $\mathbf{I}$ the identity matrix, and a, b, c, d and e coefficients.

The tensorial model obtained by taking $\gamma = \mathbf{e_x}$, the streamwise direction of the flow, $a = 0.5$, $b = -1$, and $c = d = e = 0$. Considering the studied geometry, this tensorial model is equivalent to the $H^{(4)}$ version of the AMD model proposed by Dupuy *et al.*[9,19]:

$$\tau_{ij}^{H^{(4)}AMD}\left(\mathbf{U},\overline{\Delta}\right) = H_{ij}^{(4)}\tau_{ij}^{AMD}\left(\mathbf{U},\overline{\Delta}\right), \tag{19}$$

with

$$H_{ij}^{(4)} = \begin{pmatrix}0&1&1\\1&0&0\\1&0&0\end{pmatrix}. \tag{20}$$

In this paper, the tensorial AMD model is associated with the scalar AMD model. The simulation denoted "AMDt+AMDs" is a T-LES combining the tensorial AMD model for the computation of velocity-velocity correlation subgrid term and the scalar AMD model for the density-velocity correlation subgrid term.

B. Structural modeling

Two structural models are considered in this study:

- Scale similarity model[45]:

$$\tau_{ij}^{sim} = C^{sim}\left(\widehat{\widetilde{U}_j\widetilde{U}_i}-\widehat{\widetilde{U}}_j\widehat{\widetilde{U}}_i\right), \tag{21}$$

$$\pi_j^{sim} = C^{sim}\left(\widehat{\widetilde{U}_j\widetilde{\phi}}-\widehat{\widetilde{U}}_j\widehat{\widetilde{\phi}}\right). \tag{22}$$

The scale similarity hypothesis assumes that the statistical structure of the tensor of the subgrid scales is similar to that of the smallest resolved scales. The test filter, $\widehat{\cdot}$, is explicitly computed in LES. Two test filters are considered. The simulation denoted "Sim" uses a box filter computed as an average over three cells in the three directions. In one dimension, its expression is given by:

$$\overline{\psi}(x_i) = \frac{\psi(x_{i+1})\Delta(x_{i+1})+\psi(x_i)\Delta(x_i)+\psi(x_{i-1})\Delta(x_{i-1})}{\Delta(x_{i+1})+\Delta(x_i)+\Delta(x_{i-1})}, \tag{23}$$

where $\Delta(x_i)$ is the local cell size around the point x_i. The simulation denoted "SiL" is carried out with a Laplacian filter which involves the Taylor series expansion of the box filter using the local cell size as the filter width:

$$\overline{\psi}(x_i) = \psi(x_i)+\frac{[\Delta(x_i)]^2}{24}\left.\frac{\partial^2\psi}{\partial x^2}\right|_i. \tag{24}$$

The second derivative is approximated using a second-order centered finite difference approximation.

- Gradient model[64]:

$$\tau_{ij}^{grd} = \frac{1}{12} C^{grd} \overline{\Delta_k}^2 g_{ik} g_{jk}, \tag{25}$$

$$\pi_{j}^{grd} = \frac{1}{12} C^{grd} \overline{\Delta_k}^2 g_{ik} d_k. \tag{26}$$

Unless otherwise is stated, the structural model constants used are $C^{Sim} = 1.0$, $C^{SiL} = 1.0$, and $C^{grd} = 1.0$.

C. Mixed modeling

Three mixed models are considered: (1) the multiplicative mixed model (MMG model) proposed by Dupuy *et al.*[18]; (2) a model coupling the tensorial version of the AMD model and the scale similarity model for the velocity-velocity correlation and the scale similarity associated with the scalar AMD model for the density-velocity correlation (Sim-AMDt+Sim-AMDs); (3) a combination of the scale similarity model with the WALE model (Sim-WALE+Sim-WALE). The multiplicative mixed model based on the gradient model (MMG model) is a functional model constructed such that its magnitude is expressed by the gradient model and its orientation is aligned with the rate of deformation tensor or the scalar gradient depending on the subgrid term:

$$\nu_t^{MMG}(\mathbf{g}, \mathbf{d}) = -C^{MMG} \frac{G_{kk}}{|\mathbf{S}|}, \tag{27}$$

where $C^{MMG} = 0.05$. The two other studied mixed models rely on a linear combination of the subgrid-scale stress tensors obtained with functional and structural models:

$$\tau^{mix} = A\tau^{func} + B\tau^{struc}, \tag{28}$$

where A and B are constants. τ^{func} and τ^{struc} respectively denote the subgrid-scale stress tensor modeled with functional and structural model.

IV. STUDY CONFIGURATION

A. Channel flow configuration

The study configuration is similar to the working conditions of gas-pressurized solar receivers of concentrated solar power towers. Solar receivers are supposed to be plane channels. One wall of the channel absorbs concentrated solar light whereas the other is insulated. To reproduce these conditions, thermal large-eddy simulations are performed in a fully developed three-dimensional turbulent channel flow asymmetrically heated. Fig. 1 describes the channel flow configuration. The streamwise (x) and spanwise (z) directions are periodic. The flow is bounded by two plane walls in the wall-normal direction (y). The domain size is $4\pi\delta \times 2\delta \times 4/3\pi\delta$ with $\delta = 3$mm. The temperatures of the plates are fixed to 1300 K for the hot wall ($y = 2\delta$) and 900 K for the wall representing

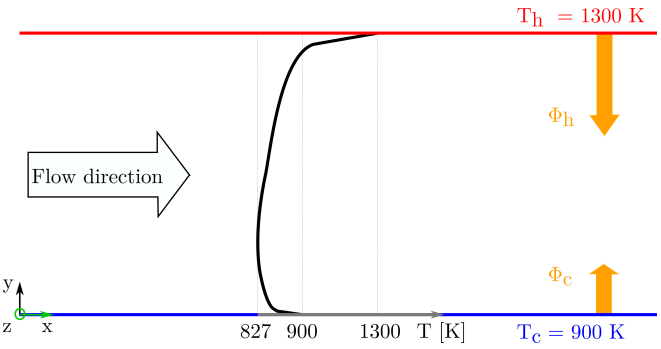

FIG. 1. Geometry of the channel flow. The periodic directions are in green.

the insulated wall and designed as "cold wall" ($y = 0$). The ratio of the wall temperatures is 1.44. Notice that, as the inertia of solar receiver walls is important, the fluid is passing through a channel at almost temporally constant wall temperatures, which justifies the choice of the thermal boundary conditions. Nevertheless, in practice, the wall temperatures are not homogeneous in the streamwise and spanwise directions. A schematic representation of the fluid temperature is given in Fig. 1. The mean fluid temperature is below the cold wall temperature, inducing heat transfers (ϕ_h and ϕ_c) oriented toward the fluid. The thermodynamical pressure, P_0, is 10 bars. A streamwise volume force is added to the channel to replicate the effect of a streamwise pressure gradient and maintain a constant mass flow rate. The hot and cold friction Reynolds numbers are respectively 640 and 1000. The mean friction Reynolds number is then 820.

B. Numerical settings

The numerical settings presented in this paper are similar to the ones described in David *et al.*[21]. The channel flow is simulated in a staggered grid system. Mesh is uniform in the homogeneous directions. In the wall-normal coordinate direction (y), it follows the hyperbolic tangent law described in Eq. 29 to capture the strong velocity and temperature gradients induced by walls.

$$y_k = L_y \left(1 + \frac{1}{a} \tanh\left[\left(\frac{k-1}{N_y - 1}\right) \tanh^{-1}(a)\right]\right) \tag{29}$$

where a is the mesh dilatation parameter and N_y is the number of grid points in the wall-normal direction. The grids employed for DNS and T-LES are listed in Tab. I. The T-LES meshes are characterized by acronyms for simplicity. The first, second, and third characters are respectively associated with the streamwise, wall-normal, and spanwise directions. "*A*" accounts for the highest resolution considered in a particular direction whereas "*D*" represents the coarsest resolution. The wall-normal resolution is not investigated because it is substantially less impacting the results than the resolution in other directions as long as the first point is in the linear region of the viscous sublayer[65]. A third-order Runge-Kutta scheme

TABLE I. Grid spacing of the DNS and T-LES meshes. The dimensionless cell sizes are computed at the cold wall (highest friction Reynolds number).

Name	Number of grid points $N_x \times N_y \times N_z$	Dimensionless cell size Δ_x^+ ; $\Delta_y^+(0)$; $\Delta_y^+(\delta)$; Δ_z^+
DNS	$1152 \times 746 \times 768$	10.9 ; 0.42 ; 5.4 ; 5.4
AAA	$192 \times 152 \times 128$	65 ; 1.1 ; 32 ; 33
BAB	$160 \times 152 \times 96$	78 ; 1.1 ; 32 ; 43
CAC	$128 \times 152 \times 72$	98 ; 1.1 ; 32 ; 58
DAD	$96 \times 152 \times 48$	130 ; 1.1 ; 32 ; 87

computes the time derivatives. Momentum convection term is discretized with a fourth-order centered scheme. The velocity divergence (representing the temperature convection in the chosen formalism), and temperature diffusion are approximated with second-order centered schemes. A Quadratic Upstream Interpolation for Convective Kinematics (Quick)[66] scheme is used for the discretization of the mass convection term. It considers a three-point upstream weighted quadratic interpolation for the cell face values. Since the scheme is based on a quadratic function it is third-order accurate in terms of Taylor series truncation error. The second-order centered scheme, employed by Streher *et al.*[44], is also considered. The simulations are performed with TrioCFD software[67].

V. RESULTS AND DISCUSSION

DNS and T-LES produce instantaneous fields. The presented results are then time-averaged and spatially-averaged in the streamwise and spanwise directions. This combination of averages is denoted by $\langle\cdot\rangle$. We address first-order and second-order statistics. Functional and mixed models are respectively traceless and partially traceless meaning that only the deviatoric Reynolds stresses can be reconstructed and compared with DNS data without filtering process[44,68]:

$$R_{ij}^{dev} = R_{ij} - \frac{1}{3} R_{kk}\delta_{ij}, \tag{30}$$

To facilitate the comparison between LES and DNS, the modeled terms are systematically added to the associated quantity.

$$R_{ij}^{DNS,dev} = R_{ij}^{LES,dev} + \langle \tau_{ij}^{SGS}(\mathbf{U},\overline{\Delta})\rangle^{dev}, \tag{31}$$

where $R_{ij}^{DNS} = \langle U_i U_j\rangle - \langle U_i\rangle\langle U_j\rangle$ and $R_{ij}^{LES} = \langle \widetilde{U}_i\widetilde{U}_j\rangle - \langle\widetilde{U}_i\rangle\langle\widetilde{U}_j\rangle$. Note that the coordinates x_1, x_2, x_3 and x, y, z as well as U_1, U_2, U_3 and U, V, W are used interchangeably for practical reasons. For the off-diagonal Reynolds stresses, Eq. 31 becomes :

$$R_{ij}^{DNS} = R_{ij}^{LES} + \langle \tau_{ij}^{SGS}(\mathbf{U},\overline{\Delta})\rangle, \text{ for i} \neq \text{j}. \tag{32}$$

The same procedure is applied to the correlations of velocity and temperature:

$$R_{i\theta}^{DNS} = R_{i\theta}^{LES} + \langle \pi_{i}^{SGS}(\mathbf{U},T,\overline{\Delta})\rangle, \tag{33}$$

with $R_{i\theta}^{DNS} = \langle U_i\theta\rangle - \langle U_i\rangle\langle\theta\rangle$ and $R_{ij}^{LES} = \langle\widetilde{U}_i\widetilde{\theta}\rangle - \langle\widetilde{U}_i\rangle\langle\widetilde{\theta}\rangle$. Here $\pi_i^{SGS}(\mathbf{U},\widetilde{T},\overline{\Delta})$ is linked to $\pi_i^{SGS}(\mathbf{U},1/\overline{\rho},\overline{\Delta})$ by the ratio r/P_0 thanks to ideal gas law.

Several normalization are used in the following of the study. The results normalized in wall units are indicated by a superscript "+": $x_i^+ = x_i U_{\tau,w}/\nu_w$, $U_i^+ = U_i/U_{\tau,w}$, $T^+ = (T_w - T)/T_{\tau,w}$, $\langle R_{ij}\rangle^+ = \langle R_{ij}\rangle/U_{\tau,w}^2$, and $\langle U_i'\theta'\rangle^+ = \langle U_i'\theta'\rangle/(U_{\tau,w}T_{\tau,w})$. The friction velocity and the friction temperature are respectively expressed as $U_{\tau,w} = \sqrt{\nu_w \partial U/\partial x_2}$, and $T_{\tau,w} = \phi_w/(\rho_w C_p U_{\tau,w})$, with ϕ_w the conductive heat flux at the wall.

A "$(^o)$" scaling is performed as follows: $y^o = yRe_\tau^{mean}/\delta$, $U_i^o = U_i/U_\tau^{mean}$, $\langle R_{ij}\rangle^o = \langle R_{ij}\rangle/(U_\tau^{mean})^2$, $T^o = (T_w - T)/T_\tau^{mean}$, and $\langle R_{\theta\theta}\rangle^o = \langle R_{\theta\theta}\rangle/(T_\tau^{mean})^2$. ^{mean} denote the averaging of the values obtained at both walls.

The semi-local scaling, denoted "$(^*)$", involves the mean local fluid properties instead of the fluid properties at the wall[69]. The normalized quantities are: $y^* = yU_{\tau,w}^*/\overline{\nu}(y)$, $U_i^* = U_i/U_{\tau,w}^*$, $\langle R_{ij}\rangle^* = \langle R_{ij}\rangle/\left(U_{\tau,w}^*\right)^2$, $T^* = T/T_{\tau,w}^*$, $\langle R_{i\theta}\rangle^* = \langle R_{i\theta}\rangle/\left(U_{\tau,w}^* T_{\tau,w}^*\right)$, $\langle R_{\theta\theta}\rangle^* = \langle R_{\theta\theta}\rangle/\left(T_{\tau,w}^*\right)^2$, with, $U_{\tau,w}^* = \sqrt{\mu_w/\overline{\rho}(y)\partial U/\partial y}$ and $T_{\tau,w}^* = \phi_w/\left(\rho_w C_p U_{\tau,w}^*\right)$

In the figures representing wall-normal profiles and involving the wall-unit or semi-local scaling, the hot and cold sides are not separated by the center plan of the channel but by the plan corresponding to zero wall-normal velocity of the DNS results. It is located at a normalized distance of $y/(2\delta) = 0.21$ from the cold wall. Hence, the cold side designs the range $0 < y/(2\delta) < 0.21$ and the region characterized by $0.21 < y/(2\delta) < 1$ is denoted hot side in the following. The hot, respectively cold, side is designed by "hs", respectively "cs" in the key of figures.

A. Validation of the numerical method

To the authors knowledge, there is no reference data in the studied conditions. For that reason, a DNS has been carried out in isothermal conditions and compared with the DNS of Hoyas and Jiménez[15] at a friction Reynolds number of 930. The mesh refinement is very close to the one selected for the anisothermal study: $\Delta_x^+ = 10.1$, $\Delta_y^+(0) = 0.39$, $\Delta_y^+(\delta) = 5.1$, and $\Delta_z^+ = 5.1$. The results are given in Figure 2. They show that both the first- and second-order statistics are in very good agreement. Furthermore, Dupuy *et al.*[70] achieved successful comparisons of the code and numerical method used with the DNS of Lee and Moser[16] at friction Reynolds numbers of 180 and 395. Toutant and Bataille[71] performed mesh convergence analysis in anisothermal conditions. Hence, these works permit validating the achieved DNS.

B. Effects of the wall heat transfer intensity

In this section, the focus is placed on the physic of the flow. Direct Numerical simulations provide very detailed results and are then suitable to investigate the effect of the high

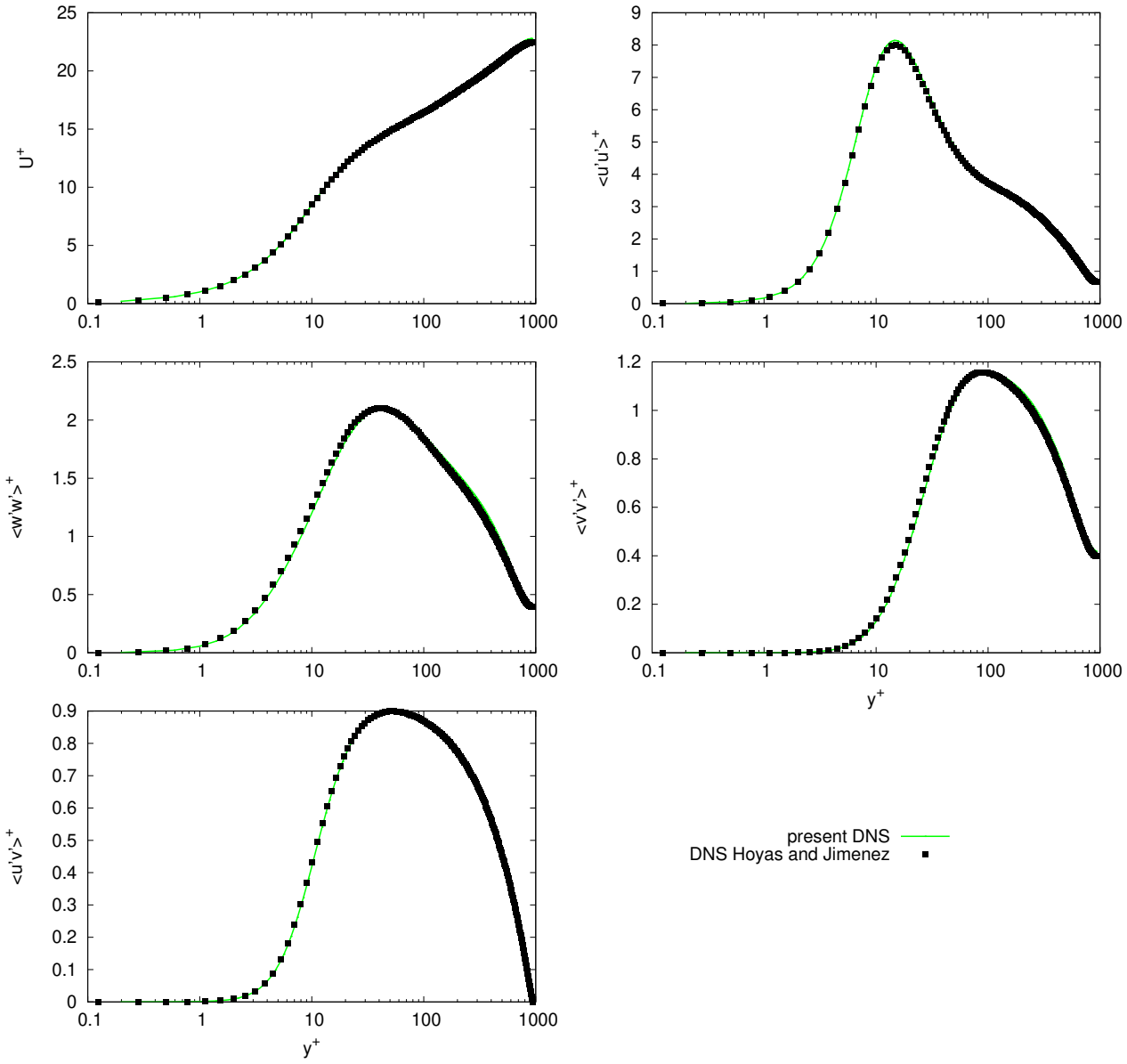

FIG. 2. Profiles of dimensionless longitudinal velocity and velocity correlations along the wall-normal direction of the channel at a friction Reynolds number of 930.

wall heat transfer on the flow. The impact of the temperature distribution obtained in the present conditions and the study of David *et al.*[21] are compared on first- and second-order statistics. In the work of David *et al.* the simulations are performed without source term in the energy equation. Hence, the fluid temperature is close to the average of the wall temperatures, meaning that the fluid is heated by one wall and cooled by the other. Thereafter, the DNS performed by David *et al.* will be denoted "DNS without source term" for simplicity. In the present study, the fluid temperature is lowered below the cold wall temperature thanks to the addition of a source term in the energy equation, see Sec. II.

The results on U, $\langle u'v' \rangle$, T, and V are presented in Fig. 3. They are normalized with the $(^o)$ scaling that is described in Section V. The streamwise velocity and the cross-correlation term are involved in the balance of the momentum equation 2. As for the temperature and the wall-normal velocity, they are involved in the balance of the energy equation 3. The results show that the location of the maximum streamwise velocity and the vanishing of the $\langle u'v' \rangle$ correlation coincide and is slightly shifted toward the hot side of the channel. On the contrary, the behavior of the temperature and wall-normal ve-

locity profiles traduce an equilibrium located on the cold side. Indeed, near $y^o = 350$, there is an inflection in the cold temperature profile, and the wall-normal velocity vanishes. The results show that lowering the fluid temperature induces a reduction of the normalized streamwise velocity in the logarithmic region and the outer layer when compared to the DNS without source term. This is explained by the higher density of the fluid in the present DNS. The streamwise velocity is higher on the cold side than on the hot side in the vicinity of the walls. Then it becomes higher on the hot side, after $y^o = 30$. The present DNS exhibits bigger peaks of the cross-correlation than the DNS without source term. This is due to the magnitude and orientation of the wall-normal velocity. The profiles of wall-normal velocity are significantly different. The magnitude of the wall-normal velocity is four times higher on the hot side than on the cold one. This is explained by the intensity of the wall heat fluxes.

The profiles of normalized temperature covariance along the wall-normal direction of the channel are given in Fig. 4. The results show that the fluctuations of temperature are highly asymmetric in the present DNS. The magnitude of the hot side peak is more than 25 times bigger than the cold peak. The central peak observed in the DNS without source term, due to the combination of the temperature gradient and the large turbulence structure in the center of the channel, is not observed in the present simulation. This is explained by the profile of fluid temperature which admit a minimum, *i.e.* a zero gradient temperature, around $y/(2\delta) = 0.21$. The minimum temperature fluctuations are observed between $y/(2\delta) = 0.08$ and $y/(2\delta) = 0.21$ because of the combination of low-temperature gradient and the weak temperature transport due to the vicinity of the wall.

The components of the Reynolds stress tensor are also compared with the DNS without source term performed by David *et al.* The semi-local scaling permits the mitigation of the asymmetry between both sides[72]. The cold side is located between the cold wall and the region where the wall-normal velocity vanishes ($y/(2\delta) = 0.21$). The rest of the channel is denoted hot side. For that reason, the hot profiles are longer than the cold profiles. In Fig. 5, the DNS results show peaks of the velocity correlations around $y^* = 15$ for the diagonal terms, corresponding to the production of low- and high-speed streaks[73]. They are due to the succeeding bursts of the low-velocity pockets near the end of the inner region which induce fast fluid motions towards the wall. These motions sweep the near-wall zone in the streamwise and spanwise directions. The fluctuations of velocities show a plateau of the spanwise velocity fluctuations in the region $70 < y^* < 200$ corresponding to the meso layer of the logarithmic region. The biggest fluctuations are those of the streamwise velocity, followed by the fluctuations of the wall-normal velocity and the fluctuations of the spanwise velocity. The peaks of these correlations are very slightly shifted toward the center of the channel when compared to the DNS without source term. Their magnitudes are, also, somewhat lower. On the hot side, this is probably due to the higher magnitude of the wall-normal velocity that tends to pull the streaks away from the wall. They are further from the hot wall and thus submitted to less shear stress which mitigates the peak of the correlation. On the cold side, the wall-normal velocity is opposed when compared to the DNS without source term, meaning that the streaks are moved towards the logarithmic region instead of being oriented closer to the wall. After, $y^* = 50$, on both sides the fluctuations of velocities are bigger in the present DNS than in the DNS of David *et al.* This agrees with the behavior of the streaks, that are moved further from the walls, discussed above. There is an inflection of the hot profiles of $\langle u'u' \rangle^*$, $\langle v'v' \rangle^*$, $\langle w'w' \rangle^*$ in the results of both DNS. In the present DNS, the inflection point is farther from the hot wall than in the DNS without source term. This is, once again, explained by the influence of the wall-normal velocity which ejects the streaks toward the outer layer. The same reason explains the difference obtained in the cross-correlation profiles. The comparison of the results provided by classical $(^+)$ scaling (Fig. 12), show that the cold side peaks are bigger than the peaks of the hot side, as usually observed in the literature (see Refs.[50,74,75]). The correlation of streamwise and wall-normal velocities exhibits peaks around $y^+ = 30$ for the hot side and $y^+ = 50$ for the cold side, which are the signature of bursting events[73]. They consist of ejections and sweeps, respectively corresponding to an outflow of low-speed fluid from the wall and inflow of high-speed fluid toward the wall[76].

The correlations involving the temperature are exposed in Fig. 6. Similarly to the velocity-velocity correlations, the DNS show peaks of $\langle u'\theta' \rangle^*$ and $\langle \theta'\theta' \rangle^*$ around $y^* = 15$. The $\langle u'\theta' \rangle^*$ cold peak is mitigated when compared to the DNS without source term. A secondary peak is observed on the hot side near $y^* = 1300$. It corresponds with the shift of the maximum velocity toward the hot side. This is not observed in the DNS without source term. The strong asymmetry of wall heat flux is responsible for this behavior. The correlation of wall-normal velocity and temperature traduces the same flow behaviors as those explained in the discussion concerning the V^o profile. This correlation vanishes exactly in the same location as the wall-normal velocity. The $\langle \theta'\theta' \rangle^*$ correlation exhibits higher peaks at the hot side than at the cold side. This is not observed in the DNS without source term of David *et al.*, in which the peak of the cold side is significantly bigger, and traduces the strong temperature gradient caused by high wall heat flux. There is an inflection of the cold side profile around $y^* = 300$. Hence, the minimum of the fluctuations is obtained closer to the cold wall than the vanishing of the wall-normal velocity. The principal peak of the correlation of the temperature observed in the DNS of David *et al.* is not reproduced in the present conditions.

The detailed results of the wall heat flux are critical since the coupling between dynamic and temperature is substantial in the studied conditions. To simplify the reading of the T-LES assessment, the DNS results on wall heat fluxes are given in the figures presented in Sec. V C 4 c. Fig. 14 exposes the probability density of normalized heat flux. On both sides, the maximum probability is reached for heat flux slightly lower than the mean heat flux.The maximum density probability is 0.04 on the cold wall whereas it is only 0.03 on the hot wall. Fig. 15 gives the instantaneous fields of both wall heat fluxes. Small red stains depict high heat fluxes while blue zones rep-

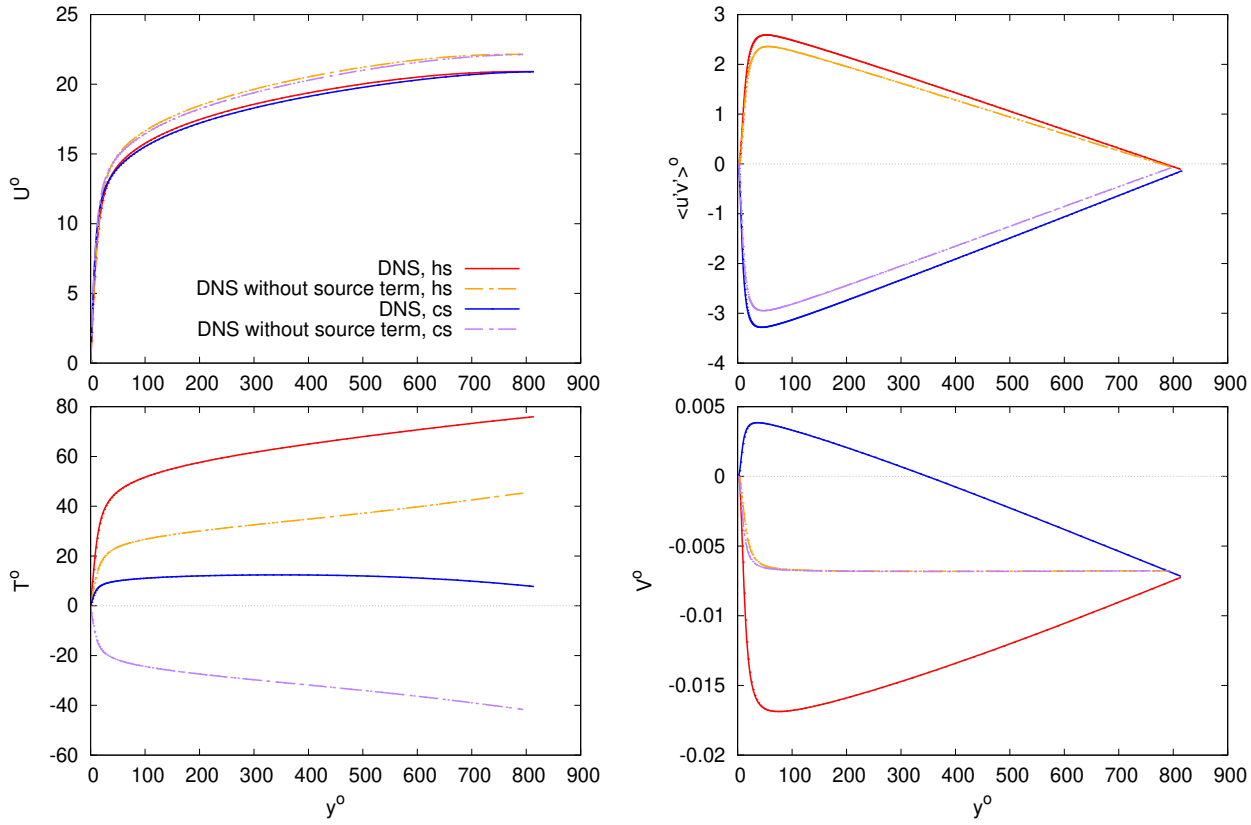

FIG. 3. Profiles of dimensionless longitudinal velocity, correlation of longitudinal and wall-normal velocities, wall-normal velocity, and temperature along the wall-normal direction of the channel.

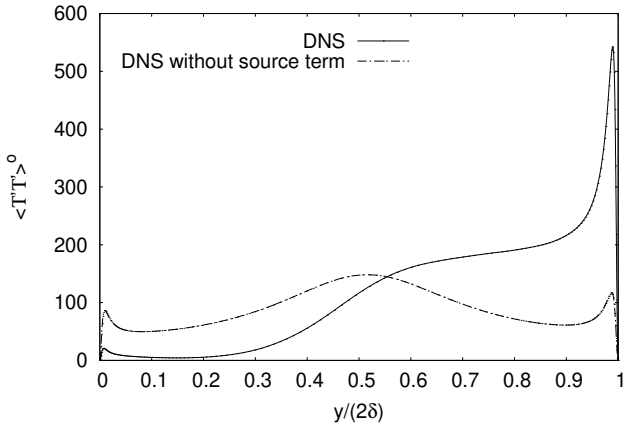

FIG. 4. Profiles of normalized temperature covariance along the wall-normal direction of the channel.

resent low heat fluxes. The DNS results show very high-frequency turbulent structures that enhance the wall-normal convection. The fluid structures at relatively low temperatures are driven in the vicinity of the wall. At the hot wall, the maximum wall heat flux reaches 1250 $\mathrm{kW/m^2}$, *i.e.* about 4.8 times the mean hot wall heat flux. On the cold side, the ratio between the maximum cold heat flux and the mean cold heat flux is 6.1. The results obtained by David *et al.*[21], without source term, show a ratio of 6.6 with a mean wall heat flux of 97 $\mathrm{kW/m^2}$. Very low heat transfer zones appear to be associated with long structures oriented toward the streamwise direction. These blue shapes are probably due to the presence of streaks above the viscous sublayer of the involved regions. The DNS results show that the ratio between the maximum wall heat flux and the mean wall heat flux is bigger at the cold wall, see Tab. IV. The ratios between the RMS of wall heat flux and the mean wall heat flux are identical and equal to 0.43 at both walls. The same ratio is obtained in the DNS of David *et al.*[21] without source term. Thus, it seems that measuring the mean wall heat flux is sufficient to determine the RMS of heat flux at this wall.

Summarizing the results on first- and second-order statistics, the conditions studied in the present paper are significantly different from the conditions investigated in David *et al.*[21]. Indeed, the wall heat fluxes are different in magnitude and direction when compared to the DNS without source term. In the present DNS, the hot wall heat flux is significantly higher than the cold wall. These differences increase the asymmetry of the flow. The both sides heating conditions then induce new flow behaviors.

In the next section, Thermal-Large Eddy simulations are

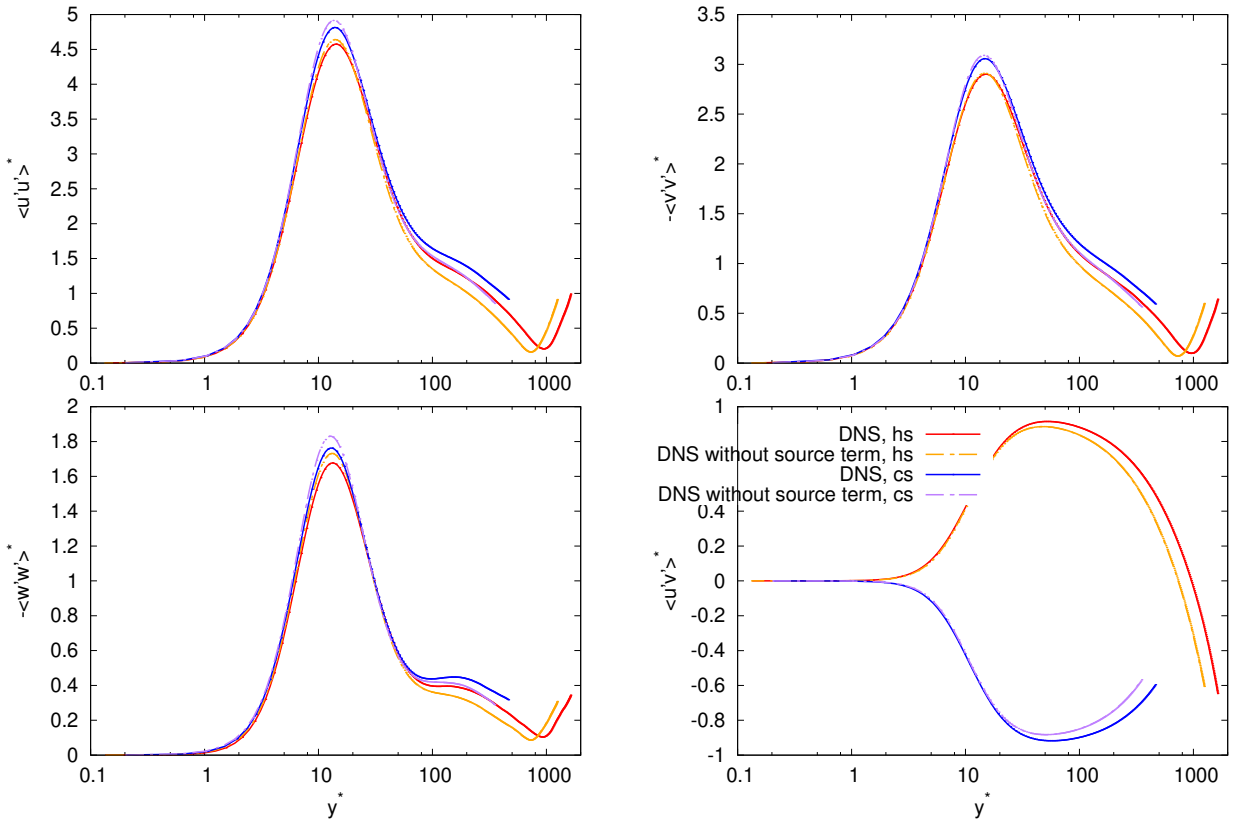

FIG. 5. Profiles of the velocity correlations in the wall-normal direction. The statistics are normalized with a semi-local scaling.

carried out and compared to DNS results in these complex but usually encountered conditions.

C. Performances of the Thermal-Large Eddy Simulations

1. *Processing of the T-LES results*

The data processing is identical to the one proposed in Ref.[21]. The DNS wall-normal profiles are interpolated on the T-LES grid to compute the T-LES error, which is computed as follows:

$$\varepsilon_X^{LES_j} = \frac{\sum_{i=1}^{N_y/2} log\left(\frac{y_{i+1}}{y_i}\right)\left|\left(X_i^{LES_j} - X_i^{DNS}\right)X_i^{LES_j}\right|}{\sum_{i=1}^{N_y} log\left(\frac{y_{i+1}}{y_i}\right)X_i^{DNS^2}} + \frac{\sum_{i=1}^{N_y/2} log\left(\frac{2\delta-y_{i+1}}{2\delta-y_i}\right)\left|\left(X_{Ny/2-i+1}^{LES_j} - X_{Ny/2-i+1}^{DNS}\right)X_{Ny/2-i+1}^{LES_j}\right|}{\sum_{i=1}^{N_y} log\left(\frac{2\delta-y_{i+1}}{2\delta-y_i}\right)X_i^{DNS^2}}, \tag{34}$$

where ε is the error, X is the observed value, LES_j refers to the jth tested model, y_i is the ith node in the wall-normal direction, and δ is the half-height of the channel. To increase the importance of near-wall phenomena, the logarithmic function is applied to the ratio between two successive points. Furthermore, the differences between LES and DNS are weighted by the local value of the quantity to accentuate the importance of the peak values.

T-LES models are assessed on 11 physical quantities divided into two groups:

- Mean quantities (first-order statistics)
  - U, the longitudinal velocity profile,
  - V, the wall-normal velocity profile,
  - T, the temperature profile,
  - ϕ, the normal conductive heat flux at the wall.
- Correlations (second-order statistics)
  - $\langle u'u'\rangle^{dev}$, the covariance of the longitudinal velocity,
  - $\langle v'v'\rangle^{dev}$, the covariance of the wall-normal velocity,
  - $\langle w'w'\rangle^{dev}$, the covariance of the transversal velocity,
  - $\langle u'v'\rangle$, the correlation of longitudinal and wall-normal velocities,

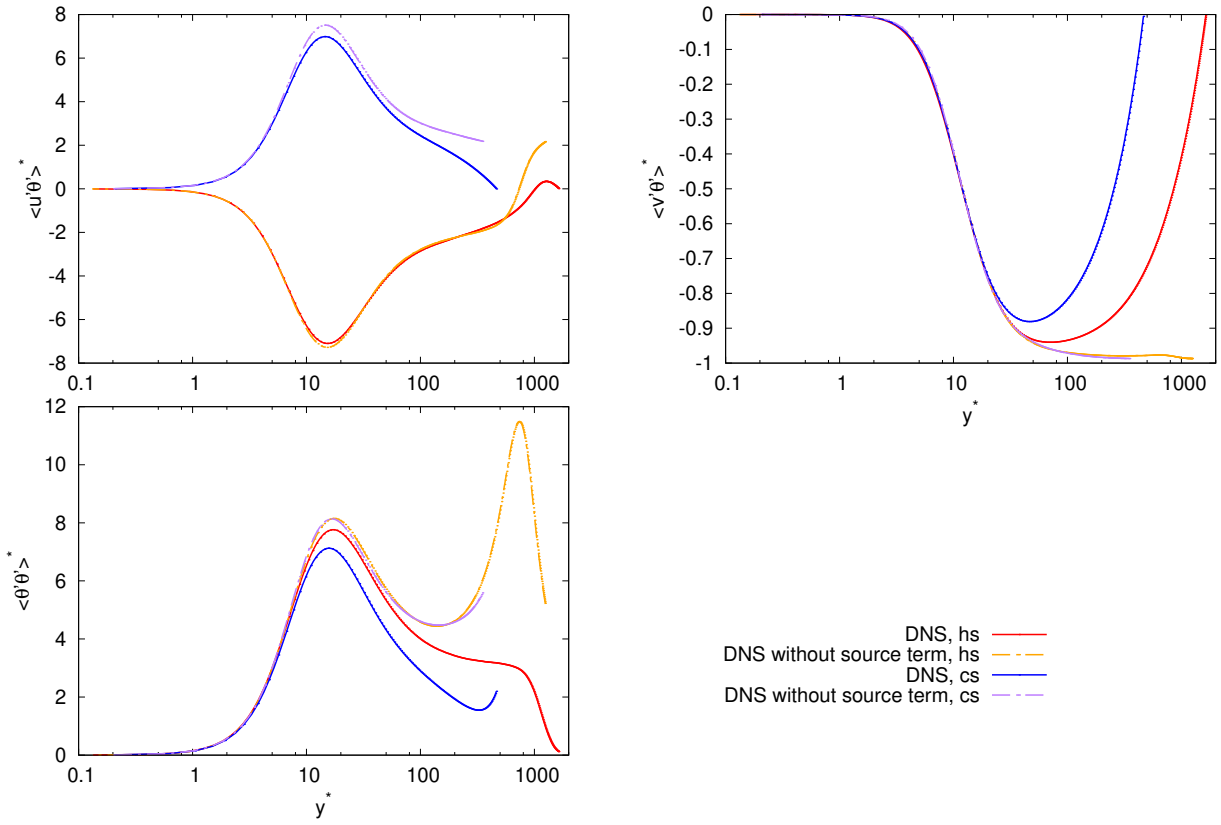

FIG. 6. Profiles of the velocity-temperature correlations and temperature covariance along the wall-normal direction of the channel. The statistics are normalized with a semi-local scaling.

- $\langle u'\theta' \rangle$, the correlation of longitudinal velocity and temperature,
- $\langle v'\theta' \rangle$, the correlation of wall-normal velocity and temperature,
- $\langle \theta'\theta' \rangle$, the covariance of temperature.

The final error of the jth T-LES model on the first-order statistics (mean quantities) is denoted Err_{mean}. The final error of the jth T-LES model on the second-order statistics (correlations) is denoted Err_{rms}. They are computed by adding the error obtained for each value and dividing this sum by the results of the worst model, *i.e.* the model that have the highest value resulting from the sum of the error on each quantity:

$$Err_{mean}^{LES,j} = \frac{\sum_X \varepsilon_X^{LES_j}}{max\left(\sum_X \varepsilon_X^{LES}\right)}, \tag{35}$$

where X is successively U, V, T and ϕ;

$$Err_{rms}^{LES,j} = \frac{\sum_X \varepsilon_X^{LES_j}}{max\left(\sum_X \varepsilon_X^{LES}\right)}, \tag{36}$$

where X is successively the square root of $\langle u'u' \rangle^{dev}$, $\langle v'v' \rangle^{dev}$, $\langle w'w' \rangle^{dev}$, $\langle u'v' \rangle$, $\langle u'\theta' \rangle$, $\langle v'\theta' \rangle$, and $\langle \theta'\theta' \rangle$.

2. *Grid sensitivity analysis*

A grid sensitivity study is performed with the four LES meshes described in Tab. I. The averaged errors on mean quantities and RMS values are presented in Fig. 7 for two T-LES. The top graph presents the error of a simulation carried out without a model ("no-model"). In this T-LES, the mass convection term is discretized with the second-order centered scheme. Note that the error committed with the DAD grid on RMS values is truncated in the graph to facilitate the reading. This error reaches 160 %. Refining the cell sizes in the x and z directions permits mitigating the error on RMS values. As for the results concerning mean quantities, the minimum errors are obtained for the "CAC" and "BAB" meshes. It signifies that the induced numerical dissipation is compensating some of the non-resolved scale effects. The results of the tensorial model ("AMDt + AMDs"), associated with the Quick scheme, are plotted on the bottom graph. Introducing a model permit to lower the error on the RMS value for all the studied grids. The results on mean quantities are slightly deteriorated when compared to the no-model simulations. For instance, the er-

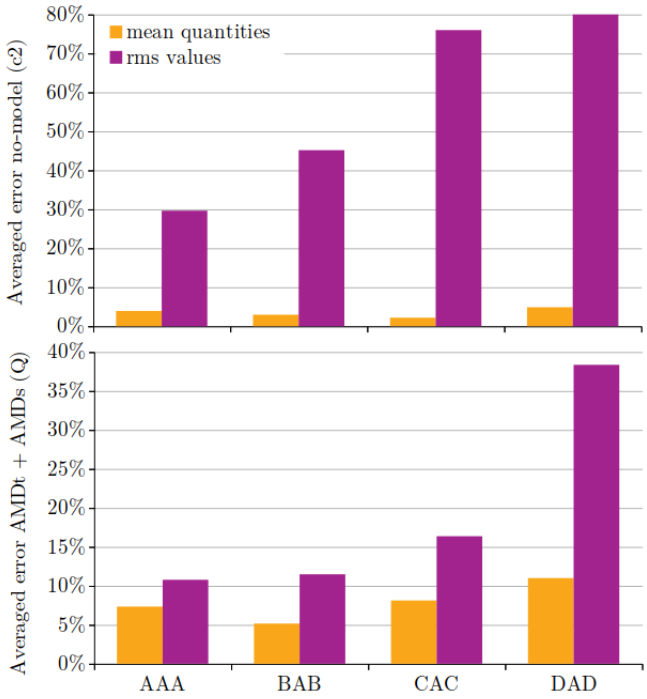

FIG. 7. Averaged errors obtained with four different meshes on mean quantities and RMS values. Simulations without model and with the tensorial AMD model are investigated.

ror committed by the no-model simulation associated with the "BAB" mesh is 3 % while the "AMDt + AMDs" simulation has 5 % of error. The "DAD" mesh produces significantly poorer results than the other grids. Regarding the error on RMS values, the "BAB" and "AAA" meshes give similar results. However, the "BAB" grid is better for the estimation of mean quantities. Overall, the "BAB" mesh seems to be the best comprise and is selected for the following of the sudy. The results are sensitive to mesh refinement as classically observed, see Ref.[19,77]. In the following, the no-model simulations carried out with the "BAB" grid are denoted ILES (for Implicit Large-Eddy Simulations).

3. *General results and assessment of LES models*

In this section, 17 T-LES are assessed on first- and second-order statistics. The justification of the model efficacy is given with the detailed results presented in Section V C 4. *A posteriori* tests allow to assess the model taking into account all the simulation factors but they do not permit to differentiate the numerical error from the model error. Moreover, scale separation is difficult to establish because the low-pass filtering arises from a complex combination of implicit filtering by the mesh and the numerical schemes. Hence, four T-LES are successively performed with the Quick scheme, denoted (Q), and the second-order centered scheme, denoted (c2) thereafter. Tab.II gives the relative errors of the T-LES on the mass flow and the friction velocity at both walls. The reference values are listed in the first line. The simulations are

TABLE II. Relative errors obtained with the T-LES on the friction velocities and the mass flow. The values are given in percentage.

Simulation	$U_{\tau,\,h}$[m/s]	$U_{\tau,\,c}$[m/s]	$\dot{m}$ [kg/s]
DNS	4.17	3.64	$1.98 \times 10^{-}2$
Simulation	$\varepsilon_{U_{\tau,\,h}}$	$\varepsilon_{U_{\tau,\,c}}$	$\varepsilon_{\dot{m}}$
AMD (Q)	-1.06	-2.51	5.25
AMD (c2)	2.77	-2.62	8.15
AMDt+AMDs (Q)	-2.41	-2.22	-6.78
WALE (Q)	-3.32	-3.49	-1.65
WALE (c2)	2.47	-2.74	3.27
Sig (Q)	-3.05	-3.26	0.01
Grd (Q)	-4.34	-3.32	-7.76
Sim (Q)	-0.94	-1.40	-0.71
Sim (c2)	3.06	-2.89	0.13
SiL (Q)	-3.45	-2.86	-5.66
MMG (Q)	-4.45	-3.50	-6.11
Sim-AMDt (Q)	-0.13	-1.77	-1.65
SiL-AMDt (Q)	-1.58	-2.12	-5.64
Sim05-WALE05 (Q)	19.31	12.83	-13.22
Sim05-WALE05 (c2)	14.12	13.72	-15.14
ILES (Q)	-4.81	-3.83	-7.16
ILES (c2)	1.77	-2.15	-1.49

performed with a fixed friction at the wall. For that reason, the friction velocity of the T-LES are very close to the wall. The mass flow is predicted within 8 % of error except for the mixed models involving the scale similarity and the WALE models which produce poor results. Note that they also significantly overestimate the friction velocities. Fig. 8 exposes the normalized errors between DNS and T-LES. Errors on mean quantities are given on the top-graph. Overall, functional models produce good results. The "Sim (c2)", "Sim-AMDt+Sim-AMDs (Q)", "SiL-AMDt+SiL-AMDs (Q)" and "ILES (c2)" simulations are also efficient. The mixed models combining the scale similarity model and the WALE model give the worst results. Regarding the second-order statistics (middle-graph), the second-order centered scheme tends to deteriorate the results except for the "Sim-WALE+Sim-WALE" simulation. The "AMDt-AMDs (Q)", denoted tensorial AMD model for simplicity, and the "SiL-AMDt+SiL-AMDs (Q)" are significantly better than the other simulations. Once again, the mixed model "Sim-WALE+Sim-WALE" is the worst. The global results, presented in the bottom-graph show the superiority of the "AMDt-AMDs (Q)" and the "SiL-AMDt+SiL-AMDs (Q)" simulations. In the following, the "AMD (Q)", the "AMDt-AMDs (Q)", the "SiL (Q)" and the "SiL-AMDt+SiL-AMDs (Q)" simulations, as well as the two ILES, are selected for the detailed analysis. Note that the "SiL (Q)" is chosen despite its poor results because it is used in the mixed model "SiL-AMDt+SiL-AMDs".

In LES, the error induced by the numerical schemes are often significant[78,79]. Thus, two numerical schemes used for the discretization of the mass convection are investigated with the ILES simulations. The results on each quantity are gathered in Tab. III. The mass convection scheme has a significant influence on all the studied quantities, except the temperature and the correlation of streamwise and wall-normal

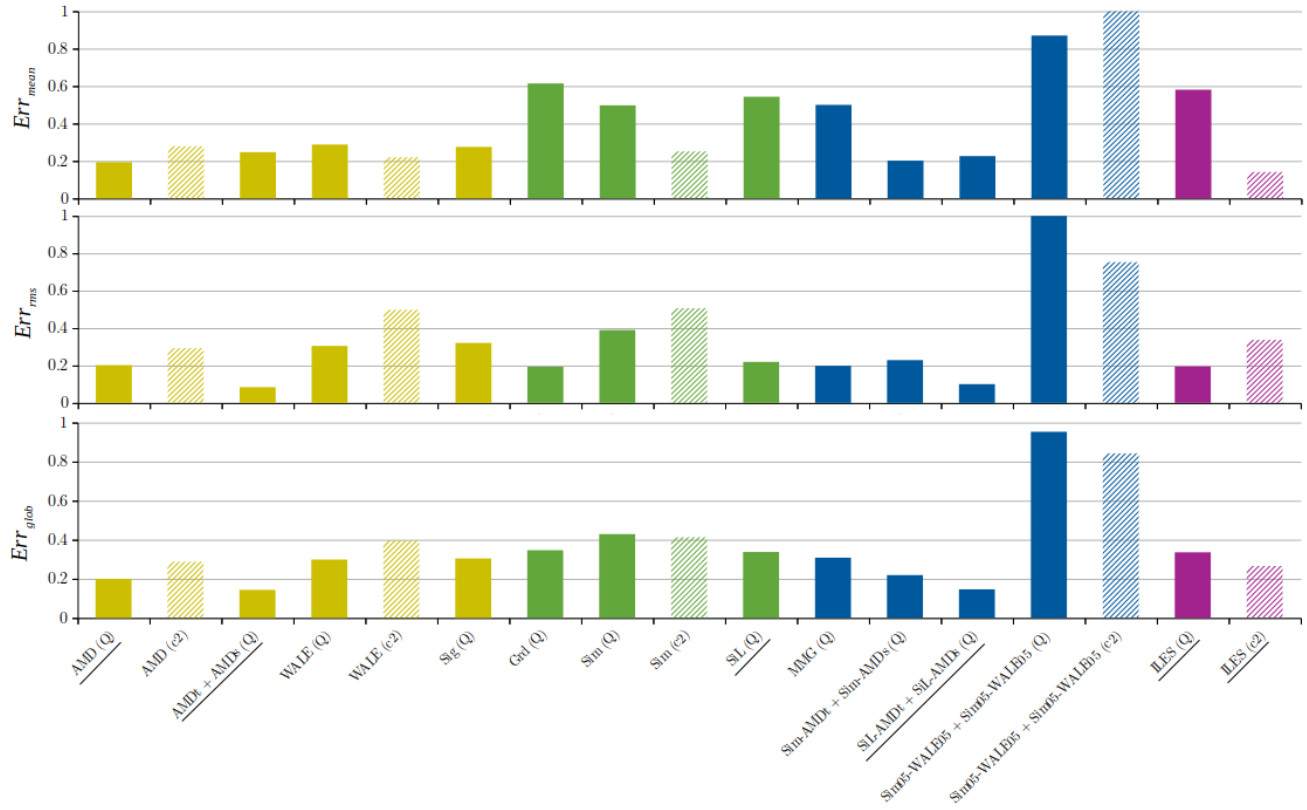

FIG. 8. Normalized error of various T-LES approaches. From top to bottom, the error concerns mean quantities, correlations, and global error. Yellow, green, and blue colors respectively stand for functional, structural, and mixed models. Purple color accounts for ILES. Full bars represent the simulations performed with the Quick scheme for the discretization of the mass convection whereas hatched bars are for T-LES using the second-order centered scheme. The six selected T-LES are underlined.

velocities. This is a major difference with the results obtained with a mean fluid temperature superior to the cold wall temperature. Indeed, David *et al.*[21] notice that the longitudinal velocity and the covariances of velocities were only quite sensitive to the numerical scheme chosen for the discretization of the mass convection term. The coupling between temperature and velocity is likely to be stronger in the present configuration. The second-order centered scheme improves the results when compared to the Quick scheme for the first-order statistics and the correlation of wall-normal velocity and temperature, as observed in Ref.[21]. The resolution error, due to the non-linearities, and the truncation error, caused by the numerical scheme, may balance each other. However, the second-order scheme substantially deteriorates the results on the diagonal terms of the Reynolds stress tensor. The higher-order term of the Quick scheme, by reducing the truncation error, is probably responsible for the better results obtained on these second-order statistics.

This section permits to assess a large number of T-LES. General results show that the best results are obtained with simulations involving functional models. Two functional models, a structural model, and a mixed model are selected for a detailed analysis.

4. *Detailed results of selected models*

In this section, the results of the selected simulations are detailed. The wall-normal profiles of first- and second-order statistics are investigated. The cold side designs the range $0 < y/(2\delta) < 0.21$, corresponding to $0 < y^+ < 420$, and the region characterized by $0.21 < y/(2\delta) < 1$, corresponding to $0 < y^+ < 1010$, is denoted hot side.

a. First order-statistics For each simulation, the relative error, computed thanks to Eq. 34, is determined for four mean quantities. The results displayed in Fig. 9 show that, except the cold wall heat flux, all the quantities are estimated within 8% of error. The temperature profile is accurately predicted. Apart from the "ILES (c2)", all the simulations give similar results on the streamwise velocity profile. The wall-normal velocity and wall heat fluxes errors are linked. Indeed, in the vicinity of the walls, the wall heat flux is similar to the temperature gradient, which is the driver of the wall-normal velocity. Hence, a poor approximation of the wall heat flux induces errors on the wall-normal velocity profile. The "SiL (Q)" and "ILES (Q)" simulations produce poor results on these quantities. On the contrary, the other simulations provide a quite good approximation of the wall-normal velocity and the hot wall heat flux. They also give a better estimation of the cold wall heat flux than "SiL (Q)" and "ILES (Q)" simulations,

TABLE III. Comparison of the numerical scheme effect on the error committed by ILES on each variable. The values are given in percentage.

	ε_U	ε_V	ε_T	ε_{ϕ_c}	ε_{ϕ_c}	$\varepsilon_{\langle u'u'\rangle^{dev}}$	$\varepsilon_{\langle v'v'\rangle^{dev}}$	$\varepsilon_{\langle w'w'\rangle^{dev}}$	$\varepsilon_{\langle u'v'\rangle}$	$\varepsilon_{\langle u'\theta'\rangle}$	$\varepsilon_{\langle v'\theta'\rangle}$	$\varepsilon_{\langle \theta'\theta'\rangle}$
ILES (Q)	7.1	8.5	1.6	35.1	8.6	39.1	29.5	60.2	6.6	17.3	10.0	20.7
ILES (c2)	1.9	3.8	1.2	6.4	1.5	77.4	60.0	116.1	8.0	23.9	1.7	29.0

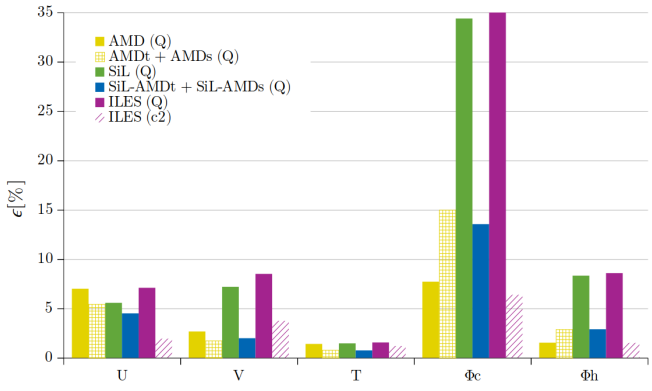

FIG. 9. Relative error on mean quantities for selected T-LES approaches. Yellow, green, and blue colors respectively stand for functional, structural, and mixed models. Full bars represent the simulations performed with the Quick scheme for the discretization of the mass convection whereas hatched bars are for T-LES using the second-order centered scheme.

even if the error on this quantity is higher than of the other. The cold wall heat flux is more sensitive to bulk temperature variations than the hot wall heat flux: even though the fluid temperature profile of T-LES is estimated within 1.6%, the error on the cold wall heat flux is relatively high.

In Fig. 10, the streamwise velocity, wall-normal velocity, and temperature profiles are plotted as functions of the wall-normal direction. Regarding the normalized streamwise velocity profile, except the "AMD (Q)", the T-LES provide a quite accurate estimation on the cold side. Note that the slope of the normalized velocity is not exactly reproduced in the log layer. On the hot side, the T-LES tend to underestimate the profile. The "AMD (Q)" is the only T-LES that overestimates the mass flow and underestimate the friction velocity, see Tab. II. As a result, it significantly overestimates the normalized streamwise velocity despite a quite satisfying approximation of the non-normalized streamwise velocity (see Fig. 9). The top-right graph describes the normalized wall-normal velocity profile. The hot side is very well approximated by the T-LES. The cold wall-normal velocity profiles are also in very good agreement with the DNS, except for the structural model and the "ILES (Q)" simulation, which overestimate this quantity. The normalized temperature profiles are plotted on the bottom graph. The "ILES (c2)" provides the best cold temperature profile among the considered T-LES. However, this simulation is not efficient in the estimation of the hot side temperature profile. Even though they tend to overestimate the profiles, the tensorial AMD model and the mixed model produce the most reliable results.

b. Second-order statistics The second-order statistics are usually analyzed in LES[46,80–82]. They facilitates the understanding of the flow behavior. Turbulence statistics are more complex to approximate for LES models than mean quantities. The correlations and covariances described in Sec. V C 1 are investigated for the six selected T-LES in Fig. 11. Apart from the tensorial AMD model and the mixed model, the diagonal terms of the Reynolds stress tensor are poorly approximated by T-LES. The results of the "ILES (c2)" simulation are very far from those of the DNS. The ranking of the T-LES is conserved between these three quantities. The spanwise velocity correlation is the most complex quantity to estimate. Globally, the $\langle u'v'\rangle$ and $\langle v'\theta'\rangle$ are well predicted by all T-LES. The correlation of the streamwise velocity and the temperature is particularly well estimated by the "AMD (Q)" simulation, which is consistent with the exact sub-filter tensor on anisotropic grids[29]. Indeed, while other models show an error of around 18%, the "AMD (Q)" has only 5% of error. Similar results are observed on the temperature-temperature correlation. The "AMD (Q)", "AMDt + AMDs (Q)", and "SiL-AMDt + SiL-AMDs (Q)" simulations produce a very good estimation of the fluctuations of cold wall heat flux. At the hot wall, the models have about 15% of error. Notice that the best results on the wall heat flux were observed on the hot side but the best estimations on the fluctuations of wall heat flux concern the cold wall. This will be discussed in Sec. V C 4 c. The "ILES (c2)" produces the worst results of all the considered simulations.

Fig. 12 exposes the velocity-velocity correlation terms. As explained in Sec. V, the deviatoric part of the diagonal terms of the Reynolds stress tensor is analyzed. The T-LES produce similar results on the correlations $\langle u'u'\rangle^{dev}$, $\langle v'v'\rangle^{dev}$, and $\langle w'w'\rangle^{dev}$. Hence, they are discussed together. The tensorial AMD model and the mixed model produce very good estimations of the hot side of the diagonal terms. On the cold side, the results of the tensorial AMD model and the mixed model are less remarkable but they are still the best among the considered simulations. These good results can be explained by the formulation of the tensorial AMD model which is able to take into account the anisotropy of the flow[19,21]. The other simulations substantially overestimate the peaks of $\langle u'u'\rangle^{dev}$, $\langle v'v'\rangle^{dev}$, and $\langle w'w'\rangle^{dev}$ on both sides. The poorly dissipative behavior scale of the similarity model induces an overestimation of turbulence statistics. The ILES, which rely on numerical dissipation, seem to suffer from the same lack of dissipation. The normalized correlations of velocities show that the scheme used for the discretization of the mass convection term affects the results, even though it is moderate. The Quick scheme, which is third-order accurate, permits reducing the overestimation of the peaks. The T-LES give a very satisfying agreement with the DNS profile of the cross-correlation

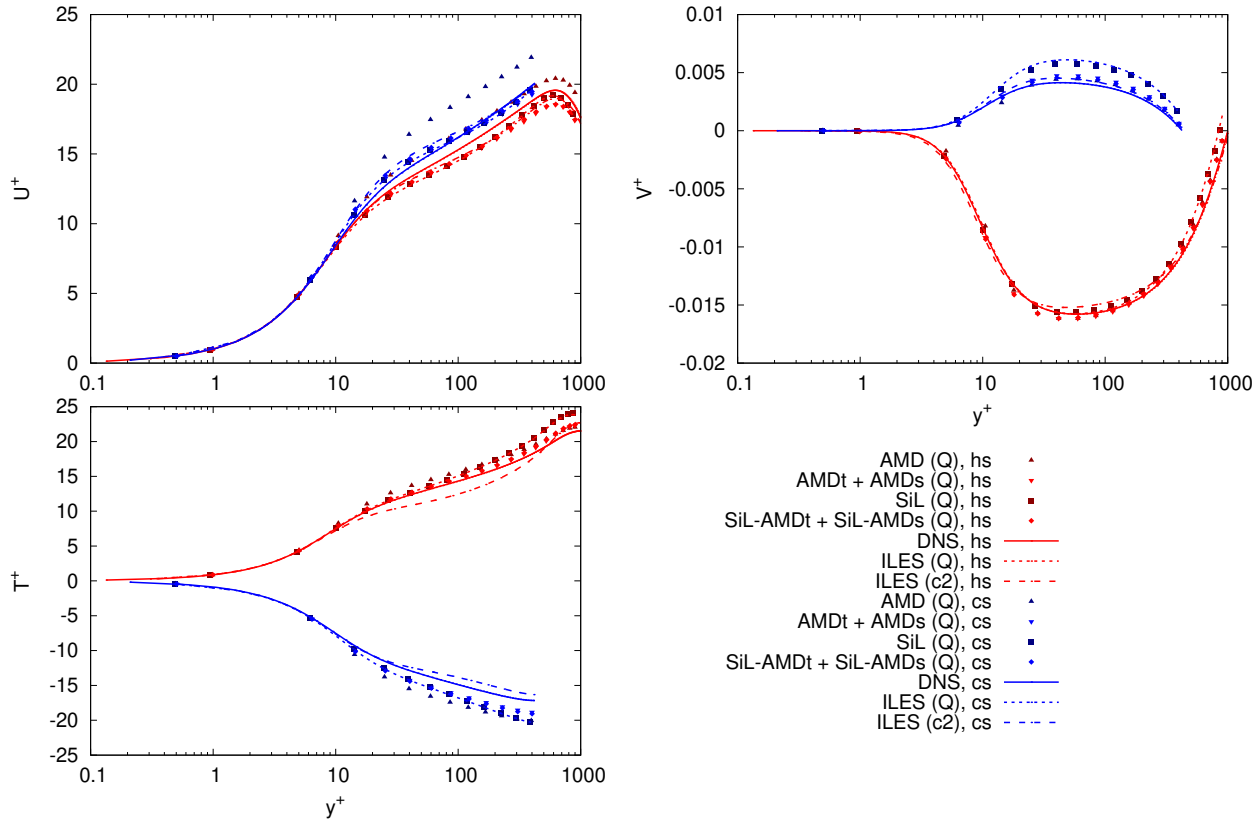

FIG. 10. Profiles of dimensionless longitudinal velocity, wall-normal velocity and temperature along the wall-normal direction of the channel.

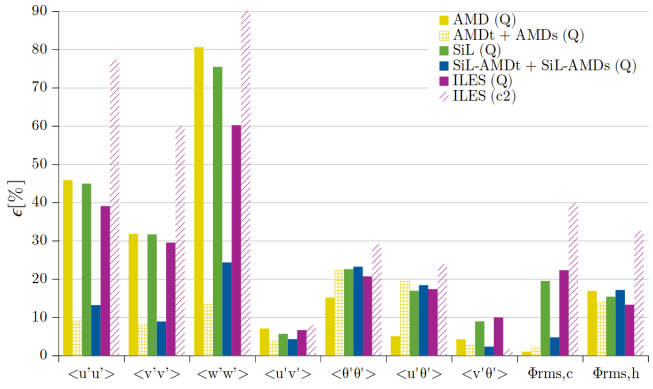

FIG. 11. Relative error on covariances for selected T-LES approaches. Yellow, green, and blue colors respectively stand for functional, structural, and mixed models. Full bars represent the simulations performed with the Quick scheme for the discretization of the mass convection whereas hatched bars are for T-LES using the second-order centered scheme.

on the cold side. On the hot side, T-LES results show a moderate overestimation. The "AMD (Q)" model predicts a peak shifted toward the center of the channel. The tensorial AMD model allows adjusting this bias.

The correlations involving the temperature are exposed in Fig. 13. The top-left graph exhibits the $\langle u'\theta'\rangle$ correlation. The hot side profile is remarkably estimated by the "AMD (Q)" model, overestimated by the simulation involving the second-order centered scheme, and underestimated by the other simulations. The mixed model has the same principal peak magnitude as the DNS. Except the ILES (c2), all the simulations reproduce the secondary peak around $y_h^+ = 750$. The correlation of wall-normal velocity and temperature is quite well predicted by all the simulations. Nevertheless, the T-LES performed with functional models overestimate the magnitude of the cold peak. The "ILES (Q)" and "SiL (Q)" simulations underestimate the fluctuations in the outer layer. The temperature covariance is displayed in the bottom graph. The "AMD (Q)" simulation produces the best results and is particularly efficient for the prediction of the cold side peak. The other simulations carried out with the Quick scheme tend to underestimate the normalized temperature covariance on both sides. This is probably due to the upwind-like construction of the Quick scheme, used for the discretization of the mass convection term, which tends to induce numerical dissipation and, thus, reduces the covariance of temperature. Particularly, the peaks of the fluctuations in the logarithmic layer are poorly reproduced. The location of the cold side profile inflection is shifted toward the center of the channel when compared to the DNS results. On the contrary, the "ILES (c2)" simulation substantially overestimates the temperature variations. Note

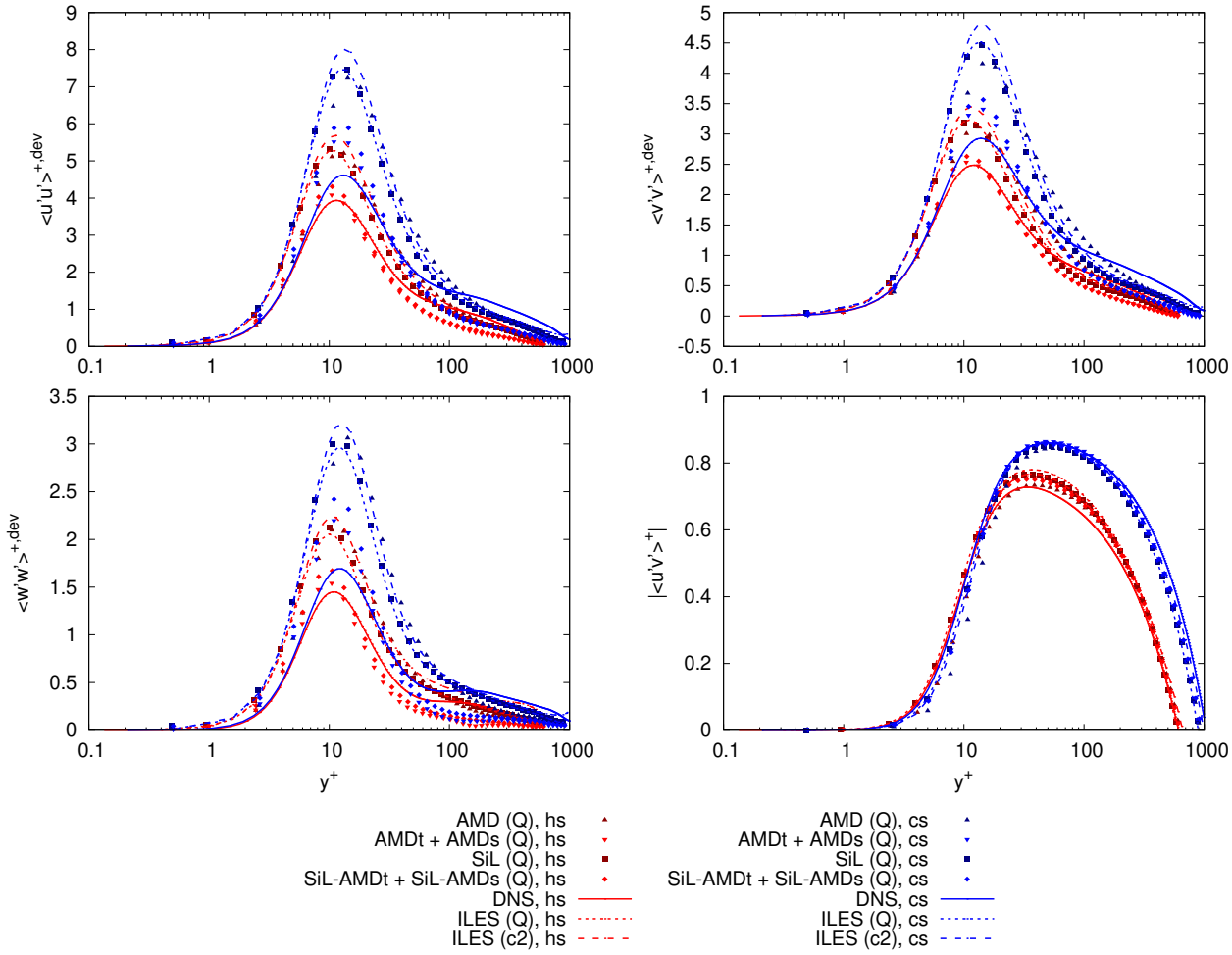

FIG. 12. Profiles of dimensionless covariances of longitudinal velocity, wall-normal velocity, transversal velocity as well as longitudinal and wall-normal velocities along the wall-normal direction of the channel. Note that the absolute value of the $\langle u'v' \rangle^+$ is plotted.

that the choice of the numerical scheme for the discretization of the mass convection term is substantially more impacting the normalized quantities involving the temperature than the normalized correlations of velocities.

c. Focus on the wall heat fluxes The wall heat fluxes estimation is a critical quantity for the design of solar receivers. For that reason, a particular attention is paid on this value.

Fig. 14 exposes the probability density of normalized heat flux. The dimensionless conductive wall heat flux is obtained with the following equation:

$$\phi_w^* = \frac{\phi_w - \phi_{w,mean}}{\phi_{plot,w,max} - \phi_{w,mean}} \tag{37}$$

where $\phi_{plot,w,max} = 3.9\phi^{DNS}_{w,\,rms} + \phi^{DNS}_{w,\,mean}$ is the biggest considered value of heat flux for plots of instantaneous wall heat flux in Fig. 15, *i.e.* 172 kW/m^2 at the cold wall and 700 kW/m^2 at the hot wall. Three instantaneous fields of wall heat flux have been averaged. The probability density of the cold wall heat flux is relatively well approximated by the "AMDt+AMDs (Q)" simulation and the mixed model despite a slight overestimation of the peak. The results of the two ILES and the "SiL (Q)" simulation show that the peak is shifted toward small values of ϕ_w^* when compared to DNS. At the hot wall, the ILES (c2) is the only simulation that predicts the good location of the peak of the probability density. All the T-LES overestimate the magnitude of the peak. The predicted distribution traduces an underestimation of the fluctuation of wall heat fluxes, confirmed by Fig. 15. Note that the "ILES (c2)" predicts a quite high probability of very strong heat flux. The strong coupling between fluid and temperature induces very high-frequency structures that are not reproduced by all T-LES.

Fig. 15 represents the instantaneous fields of both wall heat fluxes. Comparing fields of T-LES with DNS permits qualitatively assessing the models on their direct representation of the flow. The results of the "SiL-AMDt+SiL-AMDs (Q)" simulation are similar to those of the "AMDt + AMDs (Q)". For that reason, they are not displayed. The left (respectively right) graphs, corresponding to the hot (respectively cold) wall heat fluxes, are plotted in the range $0 - 700$ kW/m^2

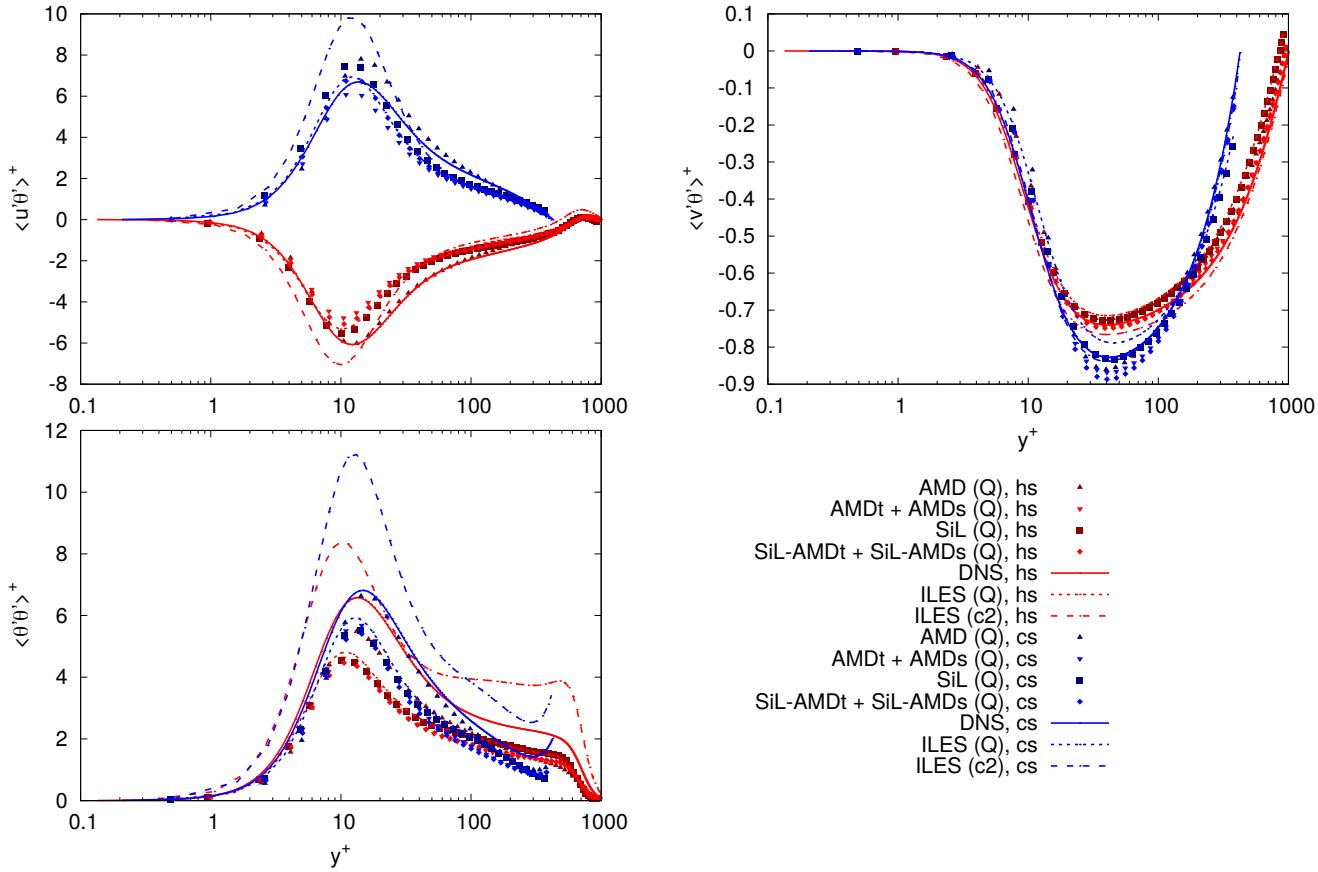

FIG. 13. Profiles of dimensionless correlations of longitudinal velocity and temperature, wall-normal velocity and temperature as well as the covariance of temperature along the wall-normal direction of the channel.

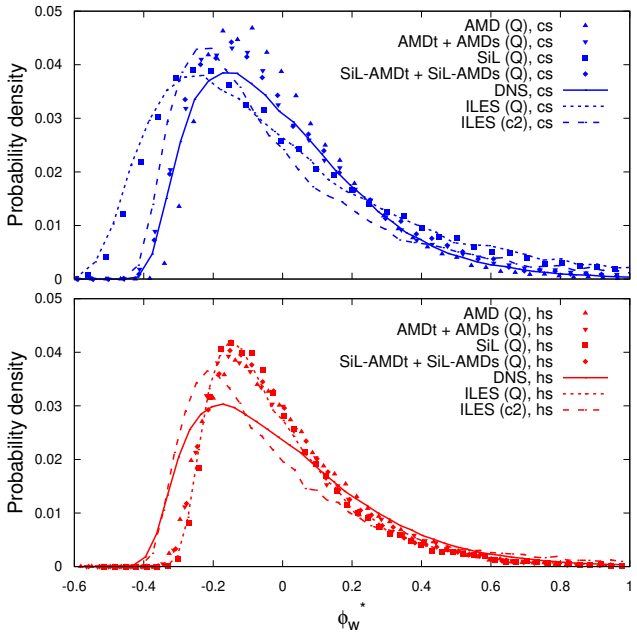

FIG. 14. Probability density of normalized heat flux.

(respectively $0-172\,\mathrm{kW/m^2}$). Small red stains depict high heat fluxes while blue zones represent low heat fluxes. Even though the mesh resolution of the T-LES is not fine enough to identify flow structures, the observed patterns of wall heat fluxes exhibit results similar to those of the DNS. The "ILES (c2)" gives a good approximation of the wall heat fluxes but the fluctuations and the maximum wall heat flux are overestimated. The T-LES slightly underestimate the mean wall hot heat flux and overestimate the cold one. The simulation involving the second order centered scheme gives an good estimation of the mean wall heat flux but overestimate the fluctuations and the maximum wall heat flux. Overall, the "AMD (Q)" and "AMDt+AMDs (Q)" simulations gives the best agreement of the patterns of wall heat fluxes.

Wall heat flux ratios are exposed in Tab. IV. The T-LES ratios of ϕ_w^{max}/ϕ_w are similar between both walls. The gap observed in DNS between the hot wall and the cold wall is not reproduced. Except the "ILES (c2)" simulation which overestimate the magnitude of the ratio between the RMS of wall heat flux and the mean wall heat flux, all T-LES tend to underestimate the magnitude of this ratio between the RMS of wall heat flux and the mean wall heat flux. This is explained by the over-dissipative behavior of the Quick scheme.

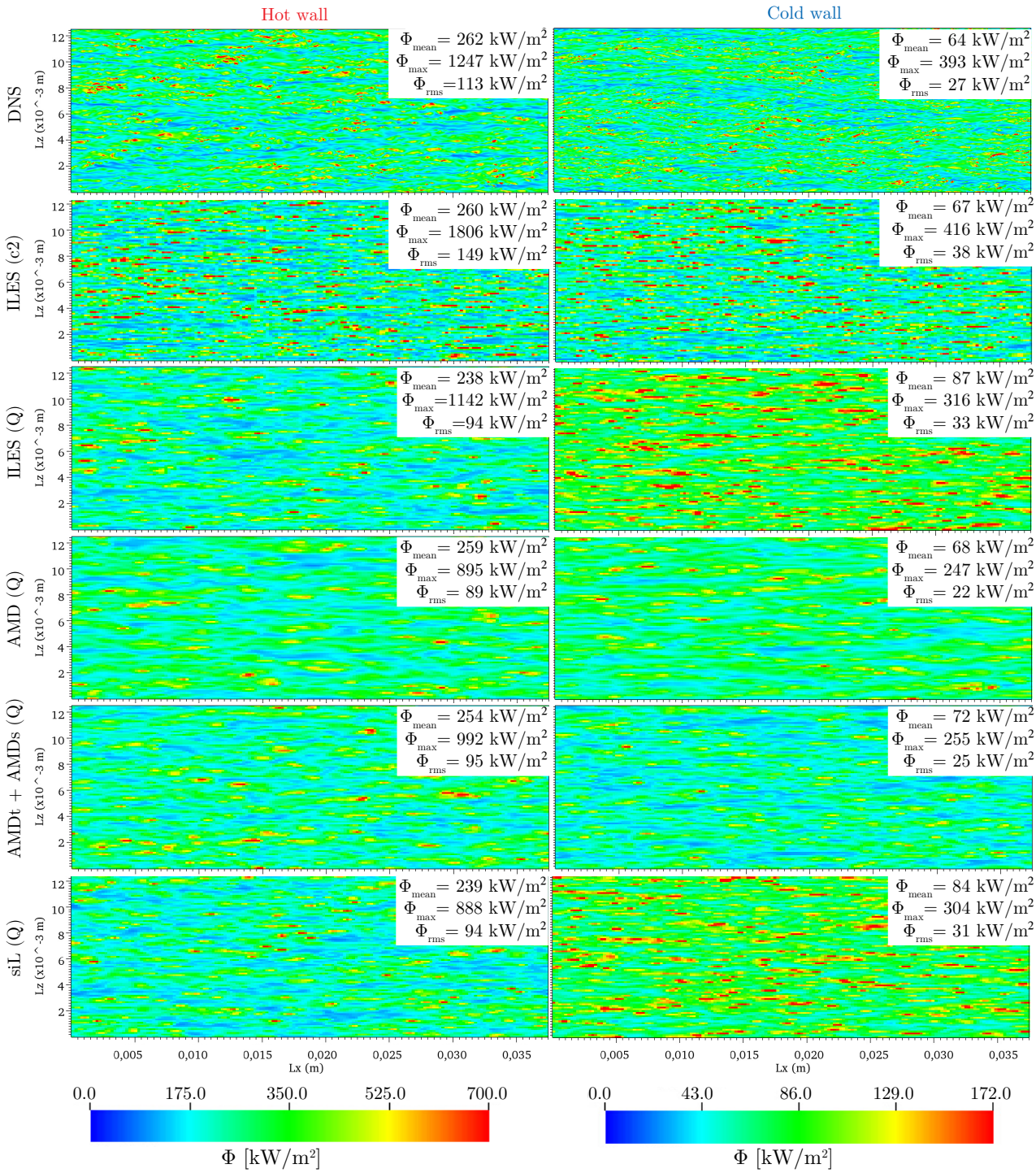

FIG. 15. Instantaneous fields of hot and cold wall heat fluxes. Pictures on the left (respectively right) side correspond to the hot (respectively cold) wall.

VI. CONCLUSION

In this study, simulations are performed in the working conditions of gas-pressurized solar receivers. The flow is highly turbulent and asymmetrically heated. A source term have been introduced in the energy equation to lower the temperature profile and generate a both side heating of the fluid. A direct numerical simulation has been performed in order to compare

TABLE IV. Wall heat flux ratios

Simulation	ϕ_h^{max}/ϕ_h	ϕ_c^{max}/ϕ_c	ϕ_h^{RMS}/ϕ_h	ϕ_c^{RMS}/ϕ_c
DNS	4.76	6.14	0.43	-0.43
AMD (Q)	3.46	3.63	0.35	-0.33
AMDt+AMDs (Q)	3.91	3.54	0.38	-0.36
SiL (Q)	3.72	3.62	0.39	-0.38
SiL-AMDt (Q)	3.82	3.59	0.37	-0.36
ILES (Q)	4.80	3.63	0.40	-0.38
ILES (c2)	6.95	6.21	0.58	-0.56

the influence of the temperature distribution with a DNS carried out by David *et al.*[21] with different thermal conditions and and flow behaviors. Indeed, in the present configuration, the asymmetrical temperature gradients induce different wall heat fluxes: the hot wall heat flux is significantly increased and the cold wall heat flux is opposed to the one obtained by David *et al.* in [21]. Furthermore, several Thermal-Large-Eddy-Simulations have been carried out and compared to the present direct numerical simulation. The considered T-LES involved functional, structural, and mixed models as well as implicit LES. A Quick scheme and a second-order centered scheme have been tested for the discretization of the mass convection term. A general assessment of 17 T-LES on first- and second-order statistics has been performed. It has led to the selection of six T-LES for a precise analysis which consisted in the detailed evaluation of four mean quantities and eight correlations. The relative error was given for each quantity and each T-LES . Furthermore, the wall-normal profiles of these quantities have been plotted and discussed. Lastly, the instantaneous fields of wall heat fluxes have been studied.

The DNS results show a very strong coupling between the dynamic of the flow and the temperature. The heating of the fluid induces wall-normal velocity. Since the fluid is asymmetrically heated by both walls, these velocities are oriented toward the center of the channel and have different magnitudes. Furthermore, the area of zero wall-normal velocity is shifted toward the geometric cold side of the channel. The minimum temperature is reached at the same distance from the walls. The quantities involved in the balance of the momentum equation show inflection or vanishing on the hot side of the channel but relatively close to the geometric center. On the contrary, the quantities involved in the balance of the energy equation exhibit these particular behaviors on the cold side, at mid-length between the cold wall and the geometric center of the channel. The intense hot wall heat flux is responsible for the high magnitude of the hot side peak of the covariance of temperature. Indeed, this peak is bigger than the cold one despite a lower local turbulence. At the hot wall, the maximum wall heat fluxes encountered are more than six-time bigger than the mean wall heat flux. The fluctuations of the heat fluxes are significant, a ratio between the mean wall heat flux and the RMS of heat flux of 0.43 is observed on both sides and seems independent of the working conditions.

Regarding the T-LES results, the ILES performed with the second-order centered scheme produce a satisfying estimation of the wall heat flux but it clearly shows a lack of dissipation. This is particularly evident when analyzing the diagonal terms of the Reynolds stress tensor, the covariance of temperature, and the instantaneous field of wall heat flux. The Quick scheme seems to reduce these issues. The simulation carried out with scale similarity model has similar drawbacks that the ILES associated with the second-order scheme even though they are less salient. Once again, we suppose that it is due to a lack of dissipation. The results also show that the hot wall heat flux is better approximated by the LES models than the cold wall heat flux. This can be attributed to the smaller temperature difference between the cold wall and the bulk temperature than between the hot wall and the bulk temperature. It is interesting to note that LES models perform better when the temperature gradient is high. The first-order statistics are, globally, better approximated than the second-order statistics for all the T-LES. Nevertheless, the correlation of the streamwise and wall-normal velocities, as well as the correlation of wall-normal velocity and temperature, are well predicted. The diagonal terms of the Reynolds stress tensor are significantly overestimated by all T-LES, except the tensorial AMD model and the mixed model which combine the scale similarity model and the tensorial AMD model. The good agreement of these models is probably due to the formulation of the tensorial AMD model which permits reproducing the anisotropy of the flow. Focusing on the instantaneous fields of wall heat flux, the functional models lead to the most reliable simulations among those considered. Summarizing all the results, the tensorial version of the AMD model is the most efficient of the considered models for the study of a channel flow asymmetrically heated from both sides. The present paper permits confirming the good results of the tensorial AMD model obtained by David *et al.* in Ref.[21].

ACKNOWLEDGMENTS

This work was granted access to the HPC resources of CINES under the allocation 2020-A0082A05099 made by GENCI. The authors acknowledge PRACE for awarding them access to Joliot-Curie at GENCI@CEA, France (PRACE Project : 2020225398). The authors gratefully acknowledge the CEA for the development of the TRUST platform. The authors gratefully acknowledge the Occitania region for their funding of the thesis grant.

DATA AVAILABILITY STATEMENTS

The data that support the findings of this study are available from the corresponding author upon reasonable request.

[1]N. Silin, V. P. Masson, D. Osorio, and J. Converti, "Hydrodynamic transition delay in rectangular channels under high heat flux," Annals of Nuclear Energy **37**, 615–620 (2010).
[2]Z. Wang, R. Zhang, T. Yu, Z. Liu, Y. Huang, J. Wang, and T. Cong, "Numerical Study on Laminar-Turbulent Transition Flow in Rectangular Channels of a Nuclear Reactor," Frontiers in Energy Research **8** (2020).
[3]M. M. Sorour and Z. A. Mottaleb, "Performances of channel-type flat-plate solar energy air-heaters," Applied Energy **18**, 1–13 (1984).

[4]S. Serra, A. Toutant, and F. Bataille, "Thermal Large Eddy Simulation in a Very Simplified Geometry of a Solar Receiver," Heat Transfer Engineering **33**, 505–524 (2012).

[5]X. Daguenet-Frick, A. Toutant, F. Bataille, and G. Olalde, "Numerical investigation of a ceramic high-temperature pressurized-air solar receiver," Solar Energy **90**, 164–178 (2013).

[6]X. Daguenet-Frick, J.-M. Foucaut, S. Coudert, A. Toutant, and G. Olalde, "Experimental Analysis of the Turbulent Flow Behavior of a Textured Surface Proposed for Asymmetric Heat Exchangers," Flow, Turbulence and Combustion **89**, 149–169 (2012).

[7]A. Colleoni, A. Toutant, G. Olalde, and J. M. Foucaut, "Optimization of winglet vortex generators combined with riblets for wall/fluid heat exchange enhancement," Applied Thermal Engineering **50**, 1092–1100 (2013).

[8]J. Kim, P. Moin, and R. Moser, "Turbulence statistics in fully developed channel flow at low Reynolds number," Journal of Fluid Mechanics **177**, 133–166 (1987).

[9]D. Dupuy, A. Toutant, and F. Bataille, "A posteriori tests of subgrid-scale models in an isothermal turbulent channel flow," Physics of Fluids **31**, 045105 (2019).

[10]O. Cabrit and F. Nicoud, "DNS of a Periodic Channel Flow with Isothermal Ablative Wall," in *Direct and Large-Eddy Simulation VII*, ERCOFTAC Series, edited by V. Armenio, B. Geurts, and J. Fröhlich (Springer Netherlands, 2010) pp. 33–39.

[11]Y. Morinishi, S. Tamano, and K. Nakabayashi, "Direct numerical simulation of compressible turbulent channel flow between adiabatic and isothermal walls," Journal of Fluid Mechanics **502**, 273–308 (2004).

[12]R. D. Moser, J. Kim, and N. N. Mansour, "Direct numerical simulation of turbulent channel flow up to Reτ=590," Physics of Fluids **11**, 943–945 (1999).

[13]J. C. D. Álamo, J. Jiménez, P. Zandonade, and R. D. Moser, "Scaling of the energy spectra of turbulent channels," Journal of Fluid Mechanics **500**, 135–144 (2004).

[14]S. Hoyas and J. Jiménez, "Scaling of the velocity fluctuations in turbulent channels up to Reτ=2003," Physics of Fluids **18**, 011702 (2006).

[15]S. Hoyas and J. Jiménez, "Reynolds number effects on the Reynolds-stress budgets in turbulent channels," Physics of Fluids **20**, 101511 (2008).

[16]M. Lee and R. D. Moser, "Direct numerical simulation of turbulent channel flow up to," Journal of Fluid Mechanics **774**, 395–415 (2015).

[17]H. Kawamura, H. Abe, and Y. Matsuo, "DNS of turbulent heat transfer in channel flow with respect to Reynolds and Prandtl number effects," International Journal of Heat and Fluid Flow **20**, 196–207 (1999).

[18]D. Dupuy, A. Toutant, and F. Bataille, "A priori tests of subgrid-scale models in an anisothermal turbulent channel flow at low mach number," International Journal of Thermal Sciences **145**, 105999 (2019).

[19]D. Dupuy, A. Toutant, and F. Bataille, "A posteriori tests of subgrid-scale models in strongly anisothermal turbulent flows," Physics of Fluids **31**, 065113 (2019).

[20]F. Aulery, D. Dupuy, A. Toutant, F. Bataille, and Y. Zhou, "Spectral analysis of turbulence in anisothermal channel flows," Computers & Fluids A Special Issue in Honor of Cecil "Chuck" E. Leith, **151**, 115–131 (2017).

[21]M. David, A. Toutant, and F. Bataille, "Investigation of thermal large-eddy simulation approaches in a highly turbulent channel flow submitted to strong asymmetric heating," Physics of Fluids **33**, 045104 (2021).

[22]Y. Zhiyin, "Large-eddy simulation: Past, present and the future," Chinese Journal of Aeronautics **28**, 11–24 (2015).

[23]P. Sagaut, *Large Eddy Simulation for Incompressible Flows*, 3rd ed. (Springer, 1998).

[24]M. H. Silvis, R. A. Remmerswaal, and R. Verstappen, "Physical consistency of subgrid-scale models for large-eddy simulation of incompressible turbulent flows," Physics of Fluids **29**, 015105 (2017).

[25]J. Smagorinsky, "General circulation experiments with the primitive equations," Monthly Weather Review **91**, 99–164 (1963).

[26]F. Nicoud and F. Ducros, "Subgrid-Scale Stress Modelling Based on the Square of the Velocity Gradient Tensor," Flow, Turbulence and Combustion **62**, 183–200 (1999).

[27]M. Kim, J. Lim, S. Kim, S. Jee, and D. Park, "Assessment of the wall-adapting local eddy-viscosity model in transitional boundary layer," Computer Methods in Applied Mechanics and Engineering **371**, 113287 (2020).

[28]F. Nicoud, H. B. Toda, O. Cabrit, S. Bose, and J. Lee, "Using singular values to build a subgrid-scale model for large eddy simulations," Physics of Fluids **23**, 085106 (2011).

[29]W. Rozema, H. J. Bae, P. Moin, and R. Verstappen, "Minimum-dissipation models for large-eddy simulation," Physics of Fluids **27**, 085107 (2015).

[30]R. Verstappen, "An eddy-viscosity model based on the invariants of the rate-of-strain tensor," in *Direct and Large-Eddy Simulation VIII*, ERCOFTAC Series, edited by H. Kuerten, B. Geurts, V. Armenio, and J. Fröhlich (Springer Netherlands, Dordrecht, 2011) pp. 83–88.

[31]H. Kobayashi, "The subgrid-scale models based on coherent structures for rotating homogeneous turbulence and turbulent channel flow," Physics of Fluids **17**, 045104 (2005).

[32]A. W. Vreman, "An eddy-viscosity subgrid-scale model for turbulent shear flow: Algebraic theory and applications," Physics of Fluids **16**, 3670–3681 (2004).

[33]F. X. Trias, D. Folch, A. Gorobets, and A. Oliva, "Building proper invariants for eddy-viscosity subgrid-scale models," Physics of Fluids **27**, 065103 (2015).

[34]S. Ryu and G. Iaccarino, "A subgrid-scale eddy-viscosity model based on the volumetric strain-stretching," Physics of Fluids **26**, 065107 (2014).

[35]O. Métais and M. Lesieur, "Spectral large-eddy simulation of isotropic and stably stratified turbulence," Journal of Fluid Mechanics **239**, 157–194 (1992).

[36]B. Aupoix, "Subgrid Scale Models for Homogeneous Anisotropic Turbulence," in *Direct and Large Eddy Simulation of Turbulence: Proceedings of the EUROMECH Colloquium No. 199, München, FRG, September 30 to October 2, 1985*, Notes on Numerical Fluid Mechanics, edited by U. Schumann and R. Friedrich (Vieweg+Teubner Verlag, Wiesbaden, 1986) pp. 37–66.

[37]K. Horiuti, "A new dynamic two-parameter mixed model for large-eddy simulation," Physics of Fluids **9**, 3443–3464 (1997).

[38]H. Lu and C. J. Rutland, "Structural subgrid-scale modeling for large-eddy simulation: A review," Acta Mechanica Sinica **32**, 567–578 (2016).

[39]B. Vreman, B. Geurts, and H. Kuerten, "On the formulation of the dynamic mixed subgrid-scale model," Physics of Fluids **6**, 4057–4059 (1994).

[40]R. Anderson and C. Meneveau, "Effects of the Similarity Model in Finite-Difference LES of Isotropic Turbulence Using a Lagrangian Dynamic Mixed Model," Flow, Turbulence and Combustion **62**, 201–225 (1999).

[41]R. Akhavan, A. Ansari, S. Kang, and N. Mangiavacchi, "Subgrid-scale interactions in a numerically simulated planar turbulent jet and implications for modelling," Journal of Fluid Mechanics **408**, 83–120 (2000).

[42]C. Meneveau and J. Katz, "Scale-Invariance and Turbulence Models for Large-Eddy Simulation," Annual Review of Fluid Mechanics **32**, 1–32 (2000).

[43]G. S. Winckelmans, A. A. Wray, O. V. Vasilyev, and H. Jeanmart, "Explicit-filtering large-eddy simulation using the tensor-diffusivity model supplemented by a dynamic Smagorinsky term," Physics of Fluids **13**, 1385–1403 (2001).

[44]L. B. Streher, M. H. Silvis, P. Cifani, and R. W. C. P. Verstappen, "Mixed modeling for large-eddy simulation: The single-layer and two-layer minimum-dissipation-Bardina models," AIP Advances **11**, 015002 (2021).

[45]J. Bardina, J. Ferziger, and W. Reynolds, "Improved subgrid-scale models for large-eddy simulation," in *13th Fluid and PlasmaDynamics Conference*, Fluid Dynamics and Co-Located Conferences (American Institute of Aeronautics and Astronautics, 1980).

[46]W.-P. Wang and R. H. Pletcher, "On the large eddy simulation of a turbulent channel flow with significant heat transfer," Physics of Fluids **8**, 3354–3366 (1996).

[47]L. D. Dailey, N. Meng, and R. H. Pletcher, "Large Eddy Simulation of Constant Heat Flux Turbulent Channel Flow With Property Variations: Quasi-Developed Model and Mean Flow Results," Journal of Heat Transfer **125**, 27–38 (2003).

[48]B. Lessani and M. V. Papalexandris, "Numerical study of turbulent channel flow with strong temperature gradients," International Journal of Numerical Methods for Heat & Fluid Flow **18**, 545–556 (2008).

[49]S. Serra, A. Toutant, F. Bataille, and Y. Zhou, "High-temperature gradient effect on a turbulent channel flow using thermal large-eddy simulation in physical and spectral spaces," Journal of Turbulence **13**, N49 (2012).

[50]S. M. Yahya, S. F. Anwer, and S. Sanghi, "Turbulent forced convective flow in an anisothermal channel," International Journal of Thermal Sciences **88**,

84–95 (2015).
[51]T. M. Eidson, "Numerical simulation of the turbulent Rayleigh–Bénard problem using subgrid modelling," Journal of Fluid Mechanics **158**, 245–268 (1985).
[52]A. Rasam, G. Brethouwer, and A. V. Johansson, "An explicit algebraic model for the subgrid-scale passive scalar flux," Journal of Fluid Mechanics **721**, 541–577 (2013).
[53]B.-C. Wang, E. Yee, J. Yin, and D. J. Bergstrom, "A General Dynamic Linear Tensor-Diffusivity Subgrid-Scale Heat Flux Model for Large-Eddy Simulation of Turbulent Thermal Flows," Numerical Heat Transfer, Part B: Fundamentals **51**, 205–227 (2007).
[54]B.-C. Wang, J. Yin, E. Yee, and D. J. Bergstrom, "A complete and irreducible dynamic SGS heat-flux modelling based on the strain rate tensor for large-eddy simulation of thermal convection," International Journal of Heat and Fluid Flow Revised and Extended Papers from the 5th Conference in Turbulence, Heat and Mass Transfer, **28**, 1227–1243 (2007).
[55]B.-C. Wang, E. Yee, D. J. Bergstrom, and O. Iida, "New dynamic subgrid-scale heat flux models for large-eddy simulation of thermal convection based on the general gradient diffusion hypothesis," Journal of Fluid Mechanics **604**, 125–163 (2008).
[56]S.-H. Peng and L. Davidson, "On a subgrid-scale heat flux model for large eddy simulation of turbulent thermal flow," International Journal of Heat and Mass Transfer **45**, 1393–1405 (2002).
[57]M. Abkar, H. J. Bae, and P. Moin, "Minimum-dissipation scalar transport model for large-eddy simulation of turbulent flows," Physical Review Fluids **1**, 041701 (2016).
[58]F. Ries, Y. Li, K. Nishad, L. Dressler, M. Ziefuss, A. Mehdizadeh, C. Hasse, and A. Sadiki, "A Wall-Adapted Anisotropic Heat Flux Model for Large Eddy Simulations of Complex Turbulent Thermal Flows," Flow, Turbulence and Combustion **106**, 733–752 (2021).
[59]S. Paolucci, "Filtering of sound from the Navier-Stokes equations." NASA STI/Recon Technical Report N **83** (1982).
[60]M. V. Papalexandris, "On the applicability of Stokes' hypothesis to low-Mach-number flows," Continuum Mechanics and Thermodynamics **32**, 1245–1249 (2020).
[61]F. Nicoud, "Conservative High-Order Finite-Difference Schemes for Low-Mach Number Flows," Journal of Computational Physics **158**, 71–97 (2000).
[62]W. Sutherland, "The viscosity of gases and molecular force," The London, Edinburgh, and Dublin Philosophical Magazine and Journal of Science **36**, 507–531 (1893).
[63]M. O. Deville and T. B. Gatski, *Mathematical Modeling for Complex Fluids and Flows* (Springer Berlin Heidelberg, Berlin, Heidelberg, 2012).
[64]A. Leonard, "Energy Cascade in Large-Eddy Simulations of Turbulent Fluid Flows," in *Advances in Geophysics*, Turbulent Diffusion in Environmental Pollution, Vol. 18, edited by F. N. Frenkiel and R. E. Munn (Elsevier, 1975) pp. 237–248.
[65]S. Rezaeiravesh and M. Liefvendahl, "Effect of grid resolution on large eddy simulation of wall-bounded turbulence," Physics of Fluids **30** (2018).
[66]B. P. Leonard, "A stable and accurate convective modelling procedure based on quadratic upstream interpolation," Computer Methods in Applied Mechanics and Engineering **19**, 59–98 (1979).
[67]C. Calvin, O. Cueto, and P. Emonot, "An object-oriented approach to the design of fluid mechanics software," ESAIM: Mathematical Modelling and Numerical Analysis - Modélisation Mathématique et Analyse Numérique **36**, 907–921 (2002).
[68]G. S. Winckelmans, H. Jeanmart, and D. Carati, "On the comparison of turbulence intensities from large-eddy simulation with those from experiment or direct numerical simulation," Physics of Fluids **14**, 1809–1811 (2002).
[69]A. Patel, J. W. R. Peeters, B. J. Boersma, and R. Pecnik, "Semi-local scaling and turbulence modulation in variable property turbulent channel flows," Physics of Fluids **27**, 095101 (2015).
[70]D. Dupuy, A. Toutant, and F. Bataille, "Study of the large-eddy simulation subgrid terms of a low Mach number anisothermal channel flow," International Journal of Thermal Sciences **135**, 221–234 (2019).
[71]A. Toutant and F. Bataille, "Turbulence statistics in a fully developed channel flow submitted to a high temperature gradient," International Journal of Thermal Sciences **74**, 104–118 (2013).
[72]A. Patel, B. J. Boersma, and R. Pecnik, "Scalar statistics in variable property turbulent channel flows," Physical Review Fluids **2**, 084604 (2017).
[73]M. Lesieur, *Turbulence in Fluids*, 3rd ed., Fluid Mechanics and Its Applications (Springer Netherlands, 1997).
[74]M. Bellec, A. Toutant, and G. Olalde, "Large Eddy Simulations of thermal boundary layer developments in a turbulent channel flow under asymmetrical heating," Computers & Fluids A Special Issue in Honor of Cecil "Chuck" E. Leith, **151**, 159–176 (2017).
[75]V. Boutrouche, E. Franquet, S. Serra, and R. Manceau, "Influence of the turbulence model for channel flows with strong transverse temperature gradients," International Journal of Heat and Fluid Flow **70**, 79–103 (2018).
[76]C. Bailly and G. Comte-Bellot, *Turbulence*, Experimental Fluid Mechanics (Springer International Publishing, 2015).
[77]F. Kremer and C. Bogey, "Large-eddy simulation of turbulent channel flow using relaxation filtering: Resolution requirement and Reynolds number effects," Computers & Fluids **116**, 17–28 (2015).
[78]S. Ghosal, "An Analysis of Numerical Errors in Large-Eddy Simulations of Turbulence," Journal of Computational Physics **125**, 187–206 (1996).
[79]B. J. Geurts, "Analysis of errors occurring in large eddy simulation," Philosophical Transactions of the Royal Society A: Mathematical, Physical and Engineering Sciences **367**, 2873–2883 (2009).
[80]S. Stolz, N. A. Adams, and L. Kleiser, "An approximate deconvolution model for large-eddy simulation with application to incompressible wall-bounded flows," Physics of Fluids **13**, 997–1015 (2001).
[81]S. Singh, D. You, and S. T. Bose, "Large-eddy simulation of turbulent channel flow using explicit filtering and dynamic mixed models," Physics of Fluids **24**, 085105 (2012).
[82]L. Wang, J. Liu, S. Hussain, and B. Sundén, "Large eddy simulation of turbulent heat transfer in a non-isothermal channel: Effects of temperature-dependent viscosity and thermal conductivity," International Journal of Thermal Sciences **146**, 106094 (2019).